
Electronic Thesis and Dissertation Repository

9-23-2022 2:00 PM

Multi-scale computational modeling of coronary blood flow: application to fractional flow reserve.

Jermiah Joseph, *The University of Western Ontario*

Supervisor: McIntyre, Christopher W., *Lawson Health Research Institute*

Co-Supervisor: Goldman, Daniel., *The University of Western Ontario*

A thesis submitted in partial fulfillment of the requirements for the Master of Science degree in
Medical Biophysics

© Jermiah Joseph 2022

Follow this and additional works at: <https://ir.lib.uwo.ca/etd>



Part of the [Cardiology Commons](#), and the [Medical Biophysics Commons](#)

Recommended Citation

Joseph, Jermiah, "Multi-scale computational modeling of coronary blood flow: application to fractional flow reserve." (2022). *Electronic Thesis and Dissertation Repository*. 8918.
<https://ir.lib.uwo.ca/etd/8918>

This Dissertation/Thesis is brought to you for free and open access by Scholarship@Western. It has been accepted for inclusion in Electronic Thesis and Dissertation Repository by an authorized administrator of Scholarship@Western. For more information, please contact wlsadmin@uwo.ca.

Abstract

Introduction. Fractional flow reserve (FFR) is presently an invasive coronary clinical index. Non-invasive CT imaging combined with computational coronary flow modelling may reduce the patient's burden of undergoing invasive testing.

Research statement. The ability to obtain information of the hemodynamic significance of detected lesions would streamline decision making in escalation to invasive angiography.

Methods. A reduced order (lumped parameter) model of the coronary vasculature was further developed. The model was used in the assessment of the roles of structure and function on the FFR. Sophisticated methods were used to elicit numerical solutions. Further, CT imaging (n = 10) provided multiple porcine geometries based upon algorithms encoded within an existing scientific platform.

Results. It was found that the length of large vessel stenosis and presence of microvascular disease are primary regulators of FFR. Further, the CT data provided a basis to investigate relationships between coronary geometry (structure) and blood flow (function) attributes.

Discussion. The presented model, upon personalization, may compliment and streamline ongoing imaging efforts by guiding FFR assessment. It is likely to assist in preliminary data generation for future projects. The computational geometries will contribute to an open source service that will be made available to our University's researchers.

Keywords: Computational fluid dynamics, coronary vasculature, lumped parameter modelling, data driven modelling.

Summary for Lay Audience

A buildup of plaque in the coronary arteries that supply blood to the heart's muscle is often fatal. To assess the severity of these buildups on the heart's blood supply, physicians measure the pressure along the artery to estimate severity by an index known as fractional flow reserve. This index is obtained by inserting a pressure wire through the patient's artery of interest and measuring the pressure before and after the plaque buildup. Although this is an invasive, expensive, and high-risk procedure, it has been shown to be very useful in assisting clinical decisions regarding whether the patient requires surgery. To avoid the invasive nature of this procedure, this thesis explores how one may use mathematical modelling of coronary blood flow to generate a virtual subject specific fractional flow reserve. One mode is the utilizing the routinely obtained using Computerized Tomography (CT) images of the coronary arteries. Using images from ten patients, the arteries and geometric properties were extracted to create both reduced order models (0D and 1D) as well as 3D representations. Using the reduced order models, this thesis explored various disease conditions and factors that may affect fractional flow reserve. Such conditions include implementing varying severities of stenosis as well as inducing microvascular disease within the patient geometries to investigate the combined effects. Our findings suggest that a spectrum of pathological conditions, several of which are outside the heart, should be accounted for in diagnosing the severity of coronary plaques.

Co-Authorship Statement

This is an original graduate thesis that I, Jermiah J Joseph, developed over the past two years. The contents of this thesis have been published in scientific journals and international conference proceedings with me as the first author. The outcomes of this thesis support a wider research programme.

I hereby declare that this thesis incorporates material that is a result of supervised research, as follows:

Chapter 2 of this thesis includes the content of a published article co-authored by Clara Sun (C.S), Ting Lee (T.L), Daniel Goldman (D.G), Sanjay R. Kharche (S.R.K), and Christopher W. McIntyre (C.W.M). Throughout the chapter, only my primary contributions towards the published article are included in the thesis and the contribution of the co-authors was through simulation and data collection aid (C.S), study design & manuscript revision (S.R.K, T.L, D.G, and C.W.M). The organization of the investigation, running of simulations, data analysis, and writing were performed by myself with the guidance of D.G and S.R.K.

Acknowledgments

I am grateful to my supervisors, Professors Christopher McIntyre and Daniel Goldman for their endless help and guidance throughout the course of my master's studies. I am also grateful to my committee member Professor Geoff Wild for his support and advice whenever needed. I am indebted to my advisor Dr. Sanjay Kharche for the past four years. The mentorship, training, and opportunities you have provided for me to grow not only as an individual, but as a student of science, were substantial in all my accomplishments thus far. I thank all my lab members for their assistance and friendship through these trying times. Notably, I'd like to thank my lab member Timothy Hunter, who helped me find my place in the Medical Biophysics community and department.

Most importantly, I would like to dedicate this thesis to my parents, Joseph Santhanpillai and Emarancia Joseph, for their continuous support and sacrifice that have provided me the opportunities to pursue my goals. Thank you both for teaching me the values that I carry every day, and teaching me to persevere in the face of uncertainty and self-doubt. To my sister Emma Joseph and her dog Luna, thank you for the unwavering support and unquestioned aid whenever I needed. To all my friends who together, made up the support system that allowed me to maintain a healthy balance in life, I am forever grateful. Thank you, Ayush, who constantly challenges me to improve and encouraged me to break out of my comfort zone. Thank you, Devanshi whose emotional and mental support, through the highs and lows of the past few years have been fundamental in my success. To everyone who have helped me get to this point so far and made this thesis possible, thank you.

Table of Contents

Abstract.....	ii
Summary for Lay Audience.....	ii
Co-Authorship Statement.....	iii
Acknowledgments	iv
Table of Contents	ii
List of Tables	v
List of Figures	vi
List of Abbreviations	ii
Chapter 1. Introduction.....	1
1.1 Cardiovascular disease.....	1
1.1 Overview of coronary circulation.....	1
1.2 Diagnostic tools used in clinical practice.....	4
1.3 Diagnostic measurements obtained in clinical practice.....	5
1.3.1 Fractional Flow Reserve.....	5
1.3.2 Quantitative Flow Ratio (QFR).....	7
1.3.3 Coronary Flow Reserve (CFR).....	8
1.3.4 Index of Microcirculatory Resistance (IMR).....	9
1.3.5 Lumped-parameter modelling equations.....	10
1.3.6 One-dimensional modelling equations.....	14
1.3.7 Three-dimensional modelling equations.....	17
1.4 Thesis Hypothesis and Aims.....	19
1.4.1 Hypothesis.....	19
1.4.2 Aims.....	19

Chapter 2. Structure (epicardial stenosis) and function (microvascular dysfunction) that influences coronary fractional flow reserve estimation.....	20
2.1 Abstract.....	20
2.2 Introduction.....	21
2.3 Materials and Methods.....	23
2.4 Results.....	30
2.5 Limitations and Future Directions.....	38
2.6 Conclusions and Discussion.....	39
Chapter 3. Image processing to generate computational coronary geometries..	41
3.1 Description of coronary CT data from the Lee lab.....	41
3.2 Semi-automatic segmentation.....	41
3.2.1 Imaging Visualization.....	43
3.2.2 Extracting of center lines from CT data.....	44
3.2.3 Blood vessel lumen segmentation.....	46
3.2.4 Construction of 1D geometries using tracked center lines and segmented blood vessel lumens.....	50
3.3 3D Finite element meshing.....	52
Chapter 4. Use of generated geometry in limited blood-flow simulations.....	53
4.1 Boundary Conditions.....	53
4.1.1 Aortic inflow boundary condition.....	53
4.1.2 Aortic outflow boundary condition.....	54
4.1.3 Coronary outflow boundary condition.....	56
4.2 Visual observation of radius.....	58
4.3 Hemodynamic 1D simulation.....	61
Chapter 5. Discussion and Conclusions.....	62
5.1 Discussion of lumped parameter model findings.....	62

5.2 Discussion of image processing to generate geometry.	64
5.3 A discussion of spatially extended (1D and 3D) modelling of fractional flow reserve and its applications.....	65
5.4 Future Work.	67
5.5 Conclusions.	69
Chapter 6. References.	71
Curriculum Vitae.	91

List of Tables

Table 1. A list of open-source hemodynamic simulation platforms.....	18
Table 2. Model parameter values. See Figure 7 for vessel connectivity. The rows are color coded to suggest the major epicardial coronaries, either LAD, LCX, or RCA.....	29
Table 3. Parameters used to compute microvascular impedances.....	30

List of Figures

Figure 1. Representative human heart geometry. The red chamber (LV) is the left ventricle. The brown chamber (RV) is the right ventricle. The translucent cyan tissue is the atrial chambers. In this thesis, epicardial arterial vessels on the LV and RV were considered. 2

Figure 2. Diagram of flow in the left and right coronary arteries relative to Aortic and left ventricular (LV) pressure. A: aortic (red) and left ventricular (black) pressure profile over two heart beats. B: Left main coronary artery (LMCA and C:) right coronary artery (RCA) flow profiles during the same two heart beats of panel A. 3

Figure 3. Caricature of pressure catheter used to determine pressure proximal to (P_a) and distal to (P_d) stenosis. The stenosis is shown as orange atherosclerotic plaque. The pressure catheter measures P_a and P_d over a few cardiac cycles. The recorded P_a and P_d are averaged to calculate FFR..... 6

Figure 4. Visual description of diffuse stenosis (left) and focal stenosis (right)²³..... 8

Figure 5. Multi-scale computational models. Lumped parameter models are described using ordinary differential equations (0D, left), one-dimensional models are axisymmetric simplifications of the Navier Stokes equations (1D, center), and three-dimensional models that rely upon 3D Navier Stokes equations (3D, right). In all models, initial conditions and boundary conditions are key to simulation of blood flow in the respective networks. 10

Figure 6. Windkessel models of terminal vasculature. a: 2-element Windkessel consisting of a capacitor (C) and a resistor (R). b: 3-element Windkessel consisting of an impedance (Z_c), a capacitor and a resistor. c: 4-element Windkessel consisting of an inductance (L), impedance, capacitor, and resistor. Estimating these parameters is part of patient-specific modelling. Also see Figure 20..... 11

Figure 7. Diagram of whole-body circulation model used. Coronary artery models developed in this thesis were coupled to this model at the aorta and vena cava. 15

Figure 8. Representative imaging drive 3D geometry of coronary arteries and aorta. The left circumflex coronary artery (LCX) is shown..... 17

Figure 9. The modelled lumped parameter coronary vasculature tree network. A. Closed loop vascular structure including tree network and functional components. See Table 2 for vessel names. Z_i ($i = 1$ to 9) represent terminal vessel impedances. Vessels as well as impedances shown in red were used in the simulation experiments. B. Typical blood vessel represented by a resistance (R_n), inductance (L_n), and a capacitance (C_n). P_{n-1} : vessel inlet pressure; Q_n : flow through vessel; P_n : pressure in vessel; Q_o : outlet flow; P_{n+1} : outlet pressure, or pressure in distal vessel. C. Symbols used in panels A, B, and elsewhere in this thesis. 25

Figure 10: Pressure profiles and FFR in the LAD (column A), LCX (column B), and RCA (column C). In all columns, top row shows non stenosed model behavior, second row shows the result of focal stenosis ($\alpha = 90\%$), and third row shows the result of downstream microvascular disease in the absence of focal stenosis ($\alpha = 100\%$; $\epsilon = 2.33$). In all panels, black lines and axis represent aortic pressure (proximal pressure) while red lines and axis represent the pressure of vessel of interest (distal pressure). Time dependent FFR is shown as orange dashed lines. 31

Figure 11. Flow profiles in the LAD (column A), LCX (column B), and RCA (column C). In all columns, top row shows non-stenosed (control) model flow, second row shows flow under focal stenosis ($\alpha = 90\%$) and the third row shows the flow under microvascular disease in the absence of focal stenosis ($\alpha = 100\%$; $\epsilon = 2.33$). 32

Figure 12. Dependence of flow rate (top row), maximum flow (middle row), and mean FFR (bottom row) on stenosis length (vertical axis, all panels) and vessel diameter (horizontal axis, all panels). Columns A, B, and C show LAD, LCX, and RCA results respectively. The black line in the bottom row demarcates the FFR = 0.8 threshold. ... 34

Figure 13. Dependence of flow rate (top row), maximum flow (middle row), and mean FFR (bottom row) on microvascular resistance increase (microvascular disease, vertical axis in all panels) and vessel diameter (horizontal axis, all panels). Columns A, B, and C

show LAD, LCX, and RCA results respectively. The black line in the bottom row demarcates the $FFR = 0.8$ threshold. 35

Figure 14. Histograms of FFR obtained from PRCC simulations (see Figure 7). Panel A shows the data for LAD, panel B for LCX, and panel C for RCA. 37

Figure 15. PRCC sensitivity of FFR to model control parameters. In all panels, the sensitivity of FFR to the six most relevant parameters are shown. Panel A shows the PRCC for LAD, panel B for the LCX, and panel C for the RCA. In all panels, HR: heart rate; fs: focal stenosis; ds: diffuse stenosis; r_0 : root radius of microvascular bed; Z_i : microvascular impedance; ϵ : microvasculature taper exponent; and $E_{sys, rv}$: systolic elastance of the right ventricle. 38

Figure 16. Summary of pipeline to generate geometries. CT image visualization: the images are visualized using scientific visualization software MITK-VTK, which provides the basis for semi-automatic user segmentation. Path planning: the platform generates a smooth vessel path based on user provided fiducial points. Segmentation: the user draws circles around cross sections using fiducial points along each vessel. Solid modelling: the paths and segmentations are combined to generate vessel surfaces and volumes. Meshing: the surfaces and volumes are both meshed as finite element meshes. Simulation: after applying appropriate boundary conditions, blood flow in the model is simulated. 42

Figure 17. Representative slices from the axial planes from an imaging dataset. Numbers in the top right corner correspond to the slice number from our dataset. The 16-bit grayscale images were visualized using an appropriate color mapping scheme for the reader. All slices show the myocardial walls, the spine, the abdominal cavity, as well as the coronary vessels. 44

Figure 18. Control points (user defined fiducial points) of the vessel and path points. The user defines control points (left) of the vessel centrelines by visual inspection. The segmentation software provides path points (right) using algorithms based on Bezier curve fitting. 45

Figure 19. Path points obtained from a dataset. The inset shows one control point identified by the user. The software extends these control points to generate multiple path points shown in the main figure that track individual blood vessels. 46

Figure 20. Example aorta segmentation. The blue points represent the determined path points along the vessel. The user drawn segmentations are shown as green closed contours. A generic contour with the user defined fiducial points in shown in red. 47

Figure 21. Segmentation of a DICOM image. In CT imaging, the contrast agents in the blood gives a signal that shows up in each DICOM image. The signal can be used to identify vessel lumen and its surface as indicated by the closed red contour. The red contour is generated by the software using the user provided fiducial points shown in green. The red contour in this figure corresponds to the red contour in Figure 20. 48

Figure 22. 1D geometry constructed using the example SWC data given on the previous page. Individual vessels are color coded using radius (cm). 51

Figure 23. Vessel contours (color coded) and solid model (gray). 52

Figure 24. Representative left ventricular pressure profile from our previous study at a heart period of 0.83 s. The diastolic pressure is 26660 mPa and the systolic pressure is 181288 mPa. The conversion factor from mPa to mmHg is a factor 1.0/1333.2 mmHg/mPa 54

Figure 25. Resistor-Capacitor-Resistor (RCR) Windkessel unit used to represent the boundary condition for aortic outflow. The red tube represents a large vessel terminal through which the boundary condition receives a flow of Q . The arteriolar resistance is represented by R_p . Microvascular capacitance and resistance are represented by C and R_d respectively. 55

Figure 26. Components of coronary outflow boundary conditions consisting of proximal resistance R_a , arterial microvascular resistance $R_{a\text{-micro}}$, venous microvascular resistance $R_{v\text{-micro}}$, arterial compliance C_a , and microvascular compliance $C_{a\text{-micro}}$ used in spatially extended modelling. 57

Figure 27. Coronary vessel radius in each of geometries 0 through 4. On each row, radius is plotted as a function of node number (left panel) and shown in a 3D diagram (right panel). These representations may assist the user to identify a stenosis location. Locations of abnormal radius are marked as X in each panel where the user might expect unusual coronary flow behavior. 60

Figure 28. Steady state simulation for a 1D geometry. Panel A is the imaging driven construction of the 3D geometry. Panel B shows the estimated FFR. 61

List of Abbreviations

CVD	Cardiovascular disease.
CAD	Coronary artery disease.
LMCA	Left main coronary artery.
RCA	Right main coronary artery.
LAD	Left anterior descending artery.
LCX	Left circumflex artery.
PET	Position emission tomography.
MRI	Magnetic resonance imaging.
ECG	Electrocardiogram.
FFR	Fractional flow reserve.
QFR	Quantitative flow ratio.
iFR	Instantaneous wave-free ratio.
CFR	Coronary flow reserve.

Chapter 1. Introduction.

1.1 Cardiovascular disease.

Cardiovascular disease (CVD) causes 30% of deaths worldwide and is a leading cause of hospitalization¹. Despite the significant medical advances. CVD-related morbidity remains alarmingly high. Coronary artery disease (CAD) causing stenosis forms a large proportion of CVD. CAD is caused by atherosclerosis, namely the intra-coronary build-up of plaque, giving rise to undesirable coronary stenosis². Untreated coronary stenosis leads to mortal angina and myocardial infarction³. Whereas CAD treatment is almost always surgical, the current success rates of the operation are unacceptable due to sub-optimal assessment of stenosis severity^{4,5}. A current clinical need is to ascertain coronary stenosis severity prior to surgical intervention that will allow better treatment planning.

1.1 Overview of coronary circulation.

Coronary arteries supply the myocardium (**Figure 1**) with vital oxygen and nutrients. The two primary coronary arteries are the first branches to extend from the aorta, namely the left main and right coronary arteries (LMCA and RCA, respectively). The LMCA and its branches supply blood to the left side of the heart, including the left ventricle and left atria. The RCA supplies blood to the right ventricle and right atria. In addition, the RCA also supplies blood to the rhythm setting sinoatrial (primary cardiac pacemaker) and rate-controlling atrioventricular (secondary cardiac pacemaker) nodes. The LMCA branches into the left anterior descending artery (LAD) and the left circumflex artery (LCX). The LAD and its branches supply blood to the anterior wall of the left ventricle while the LCX supplies most of the left atrium, the posterior and lateral walls of the left ventricle. Whereas left and right cardiac perfusion are often times closely linked to left and right

branches, it is clinically important to know the branch dominance to better design treatments.

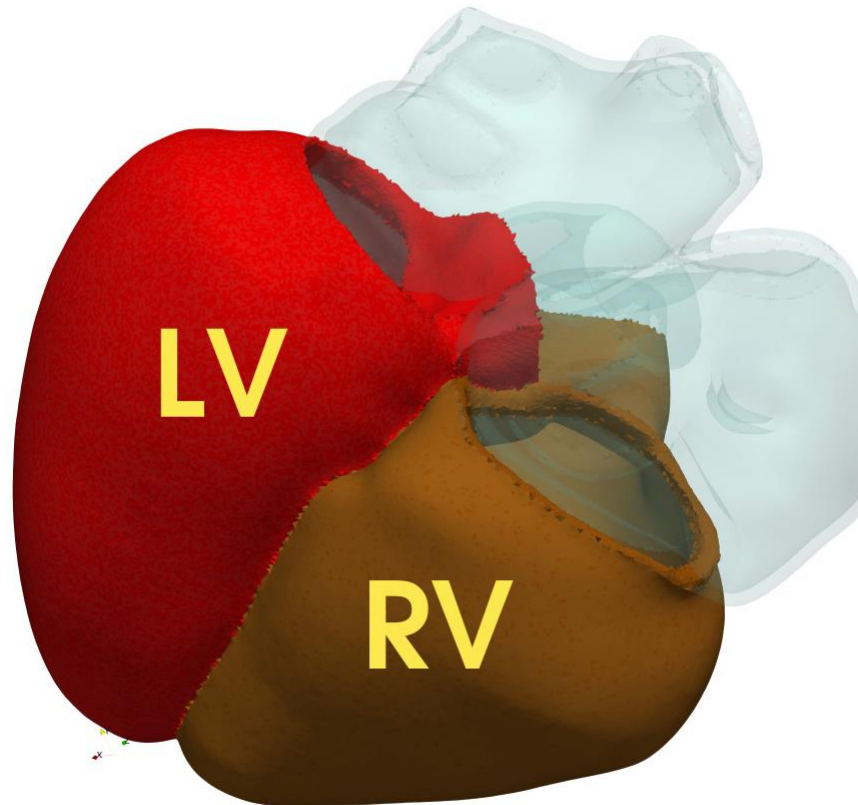


Figure 1. Representative human heart geometry. The red chamber (LV) is the left ventricle. The brown chamber (RV) is the right ventricle. The translucent cyan tissue is the atrial chambers. In this thesis, epicardial arterial vessels on the LV and RV were considered.

A distinctive attribute of coronary blood flow is its intramyocardial pressure driven phase shift with respect to the coronary pressure⁶. Intramyocardial pressure is generated by the

left ventricular pressure, myocardial fibre stress, as well as radial contraction of the myocardium⁷.

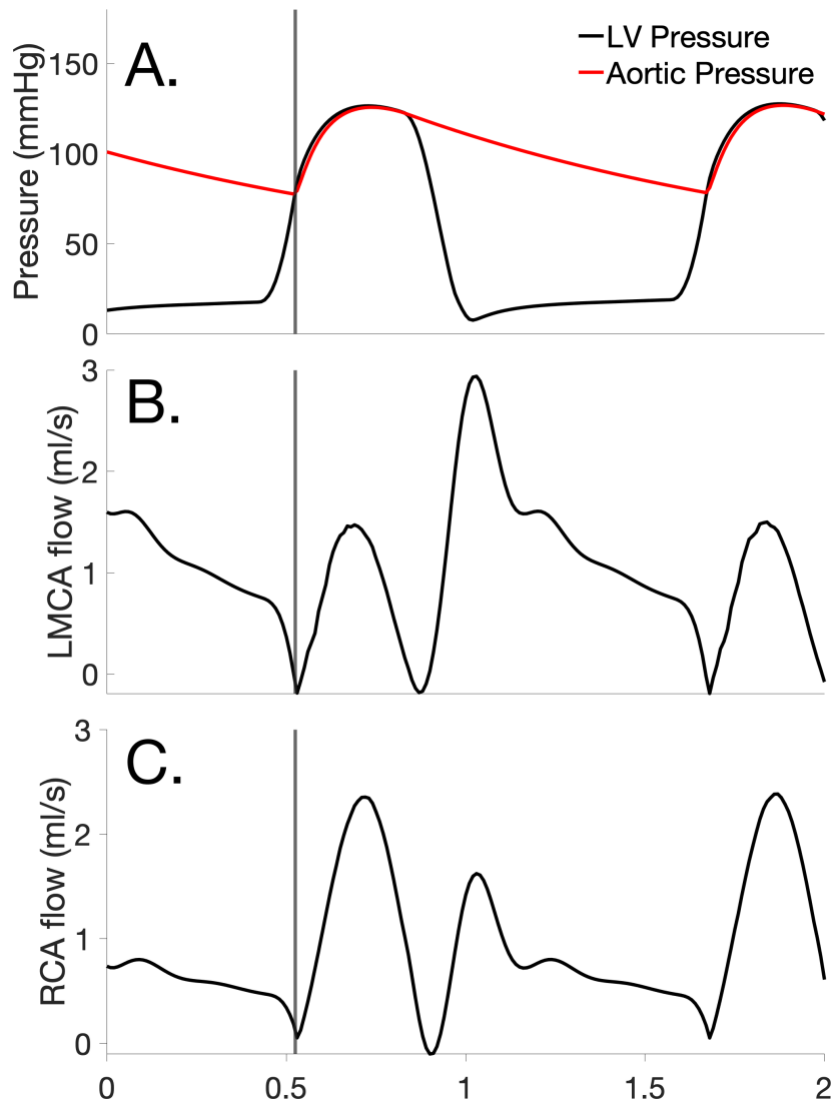


Figure 2. Diagram of flow in the left and right coronary arteries relative to Aortic and left ventricular (LV) pressure. A: aortic (red) and left ventricular (black) pressure profile over two heart beats. B: Left main coronary artery (LMCA and C:) right coronary artery (RCA) flow profiles during the same two heart beats of panel A.

The flow from the left coronary artery is low during cardiac systole (isovolumetric contraction, high intramyocardial pressure) and higher during cardiac diastole (heart relaxation, low intramyocardial pressure). As the pressure of the right ventricle is lower than that of the left ventricle, the flow in the RCA does not reduce to zero, and rather has a slight decrease (**Figure 2**).

1.2 Diagnostic tools used in clinical practice.

Currently, diagnostic tests for CAD can be divided into either non-invasive or invasive tests. Non-invasive diagnostic tests are further divided into two categories: functional tests and anatomic tests. Functional tests include exercise electrocardiography (ECG), exercise/pharmacologic stress echocardiography, exercise/pharmacologic cardiac nuclear imaging with single photon emission computed tomography (SPECT) or positron emission tomography (PET), pharmacologic stress magnetic resonance imaging (MRI), computed tomography (CT) perfusion, and CT or Doppler ultrasound-derived flow reserve measurements. There is also increasing interest in non-invasive anatomic tests, including coronary magnetic resonance angiography (MRA) and coronary artery calcium scoring. Invasive testing includes intravascular ultrasound, blood testing (to find pathological levels of troponin and creatine kinase, C-reactive protein, fibrinogen, homocysteine, lipoproteins, triglycerides, brain natriuretic peptide prothrombin), and invasive coronary angiography.

Exercise ECG involves recording the heart's electrical activity response to exercise as a stressor. This method is widely used since it does not require intravenous access or expose the patient to radiation. However, the limitations of this method include patient inability to perform adequate amounts of exercise to induce stress and possible false positives due to pharmacology⁸.

Cardiac PET is an imaging technique used to establish myocardial viability and perfusion^{9,10}. It involves cardiac imaging using a radioactive metabolite enhancement.

Cardiac PET's limitation is its reliance on high radiation doses.

Cardiac MRI is another imaging modality that uses radio frequency waves and strong magnets. It allows for 3D visualization and viewing angles from various anatomical planes. Cardiac MRI is a sophisticated technology which has high sensitivity and specificity^{11,12}. MRI does not expose patients to radiation but provides a lower resolution than PET. In addition, MRI is often unavailable due to high operational costs.

Coronary CT angiography is the most commonly used invasive method for CAD diagnosis¹³. Due to its high resolution and reproducibility, CCTA is widely used to provide 3D vasculature structure that informs the clinician regarding severity and location of stenosis.

Intravascular ultrasound utilizes a catheter and imaging to determine vessel and lumen dimensions, plaque burden and morphology. By imaging the interior of vessels, the vessel diameter and lesion lengths are determined. In addition, the composition of plaque can be determined to evaluate CAD severity and progression over time¹⁴⁻¹⁶.

It is apparent that modern biomedical diagnostics is advanced and provides large data.

This large data remains to be thoroughly exploited to benefit the critically ill patient¹⁷.

1.3 Diagnostic measurements obtained in clinical practice.

1.3.1 Fractional Flow Reserve.

A quantitative measure of aberrant coronary hemodynamics must be used to make clinical decisions regarding surgery such as revascularization. The current gold standard diagnostic tool is fractional flow reserve (FFR) estimated using intracoronary angiography

pressure measurements. FFR is defined as the ratio of maximal blood flow in a stenosed artery to the theoretical maximum in the absence of the stenosis. FFR represents the ability of an artery to maintain supply to the appended myocardium under stress which is often a precursor to ischemia. In practice, FFR is measured by inserting a pressure wire into the suspected stenosed artery to determine the ratio of the pressure distal to and proximal to the stenosis (**Figure 3**),

$$FFR(t) = \frac{P_d(t)}{P_a(t)} \quad \text{equation (1).}$$

where P_d and P_a are the stenosis related distal and proximal pressures respectively.

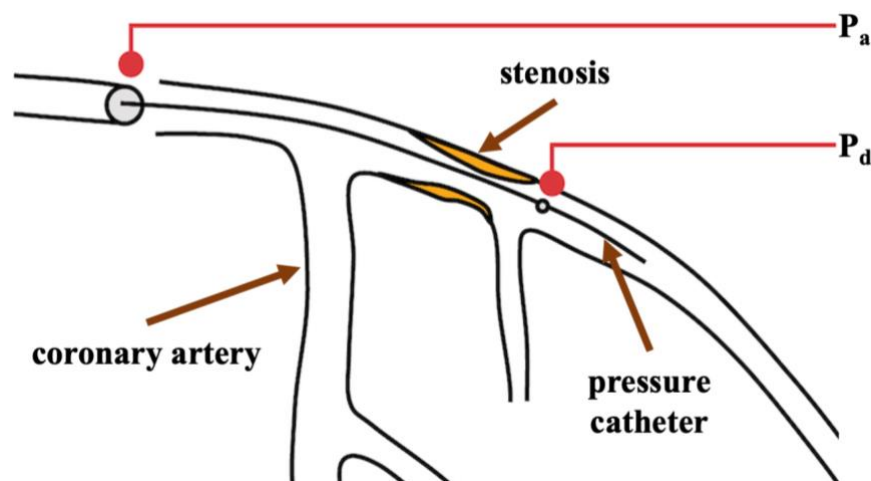


Figure 3. Caricature of pressure catheter used to determine pressure proximal to (P_a) and distal to (P_d) stenosis. The stenosis is shown as orange atherosclerotic plaque. The pressure catheter measures P_a and P_d over a few cardiac cycles. The recorded P_a and P_d are averaged to calculate FFR.

The clinically defined lower threshold for FFR is 0.8¹⁸⁻²⁰ below which percutaneous coronary intervention must be prescribed. Although FFR has been shown to identify functionally significant stenoses, the catheter lab clinical measurement of FFR is cost prohibitive and the procedure itself poses a pharmacological and surgical risk to the patient¹⁹.

With the advancement of imaging modalities, the computation of FFR through non-invasive methods have been investigated. The currently accepted method for calculating FFR non-invasively is based upon coronary computed tomographic angiography (CCTA) and is called FFR_{CT}²¹.

The two types of stenosis focused on in this thesis are diffuse and focal (**Figure 4**). In this thesis, a focal stenosis is defined as a sudden narrowing of the blood vessel (due to blockage) and a diffuse stenosis is defined as a smooth, long, narrowing of the coronary vessel (typically 20-30mm) with varying severity²².

1.3.2 Quantitative Flow Ratio (QFR).

Whereas FFR_{CT} informs the clinician about the hemodynamic severity of the epicardial vessel stenosis, quantitative flow ratio (QFR) is a novel technique that estimates coronary stenosis severity using quantitative coronary angiography imaging data. This method estimates the pressure drop across the stenosis through 3D reconstructions of quantitative coronary angiography images and a virtual hyperemic flow profile without the need for physically inducing hyperemia in patients²⁴.

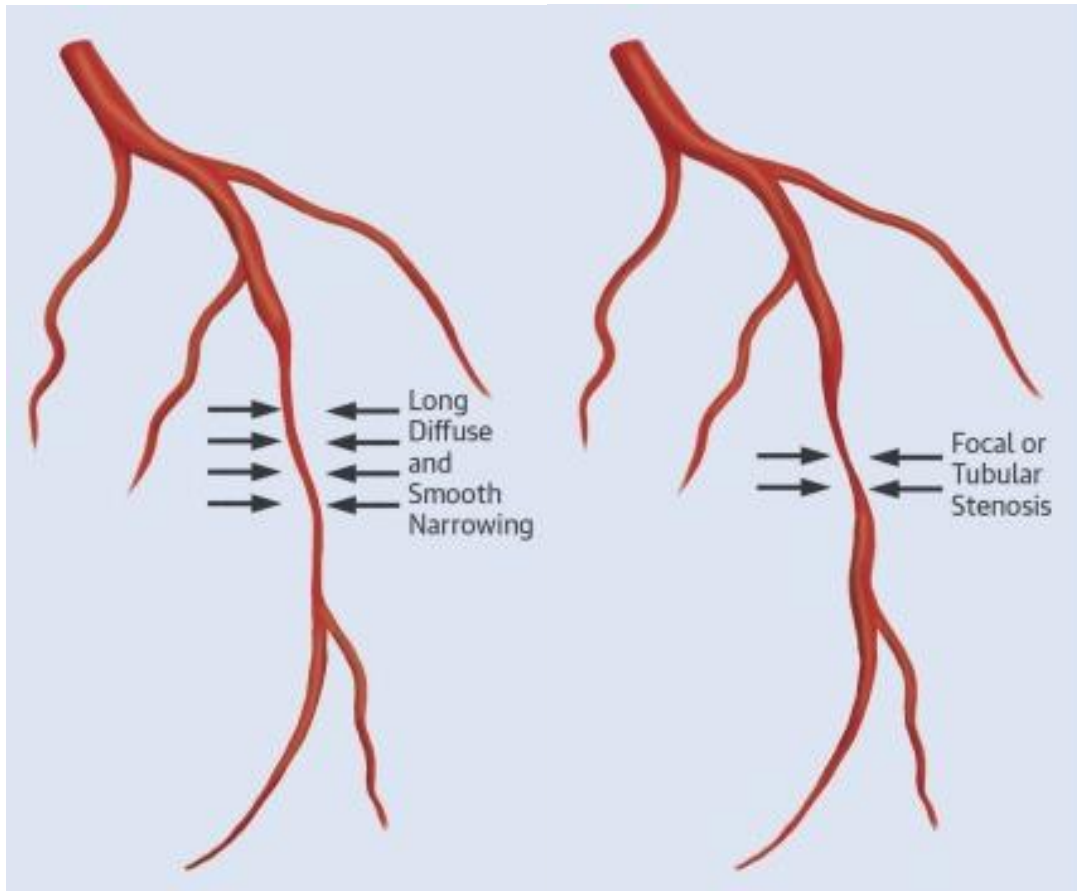


Figure 4. Visual description of diffuse stenosis (left) and focal stenosis (right)²³.

1.3.3 Coronary Flow Reserve (CFR).

Coronary flow reserve (CFR) is another coronary health index that provides wider extra coronary information such as the presence of chronic kidney disease²⁵. It is therefore crucial to ascertain coronary flow reserve index. CFR is defined as the maximum flow through a coronary artery normalized by the control flow at rest. In the case of stenosis, this measurement is obtained by calculating the maximal flow through the stenosed artery normalized by the flow through the same artery in the absence of stenosis. In the context of hemodynamic modelling, the CT imaging data may provide the stenosed vessel geometry. Using advanced computational geometry manipulation tools, the stenosed vessel geometry is manipulated to provide a normal vessel geometry. The two geometries

are then used in hemodynamic simulations to provide flow under stenosed and normal conditions.

1.3.4 Index of Microcirculatory Resistance (IMR).

The index of microcirculatory resistance (IMR) is a simple pressure wire-based measurement that provides an estimation of the where the microcirculatory resistance is minimal in a targeted coronary vasculature region²⁶. True IMR is calculated as

$$IMR = P_a \times T_{mn} \times \frac{P_d - P_w}{P_a - P_w} \quad \text{equation (2).}$$

where P_a = mean proximal coronary pressure, T_{mn} = mean hyperemic transit time, P_d = mean distal coronary pressure, and P_w = coronary wedge pressure.

Governing equations.

As in other quantitative fields of research, hemodynamic models are described using equations and inequalities. The equations represent mechanistic relationships between vessel geometry, and blood flow and pressure. The mechanism strength is dictated by modelling parameters. Experimental and clinical observations are used to identify modelling parameters, thus making the model subject specific. As illustrated in **Figure 4**, the current generation of hemodynamic models are classified into lumped-parameter, one-dimensional, and three-dimensional models. While the first is described using ordinary differential equations representing an equivalent electrical circuit, the latter two are described using partial differential equations. Brief descriptions of the equations used in lumped-parameter, 1D, and 3D modelling are provided in the following sections.

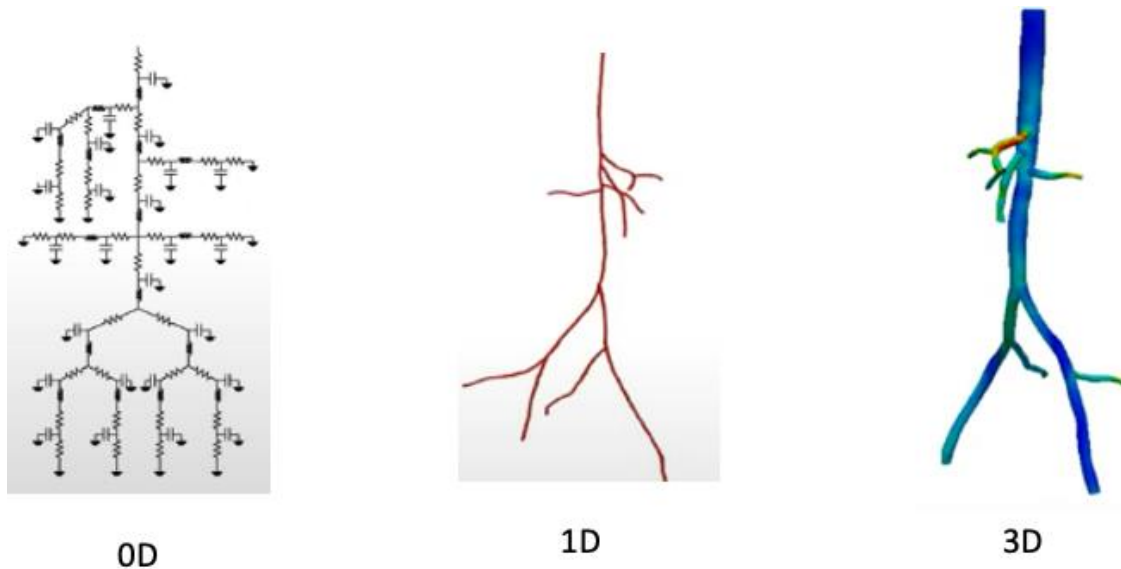


Figure 5. Multi-scale computational models. Lumped parameter models are described using ordinary differential equations (0D, left), one-dimensional models are axisymmetric simplifications of the Navier Stokes equations (1D, center), and three-dimensional models that rely upon 3D Navier Stokes equations (3D, right). In all models, initial conditions and boundary conditions are key to simulation of blood flow in the respective networks.

1.3.5 Lumped-parameter modelling equations.

Lumped-parameter models of single vessels are illustrated in **Figure 6**. These models describe relationships among hemodynamic variables using electrical circuit analogies. The primary analogies are the representation of blood flow by current and pressure by voltage. Although lumped-parameter models do not have spatial variables, they are useful for modeling global characteristics of the cardiovascular system. These models are especially suitable for representing a large portion of a closed-loop system or terminal

and complex parts of the cardiovascular system such as the heart, venous circulation, and capillary beds.

The simplest model of a blood vessel to date is the two element Windkessel model²⁷, where peripheral resistance of a blood vessel is represented by an electrical resistor and the total arterial compliance is represented by a capacitor (**Figure 6, a**). More information can be described by including a third element, a resistor characterizing the impedance, in series with the previous 2-element Windkessel (**Figure 6, b**). With the introduction of the inertance of blood in the vessel as another element, the 4-element Windkessel model was established (**Figure 6, c**). The model by Pietrabissa et al (1996) was one of the early lumped parameter descriptions of the coronary blood flow²⁸.

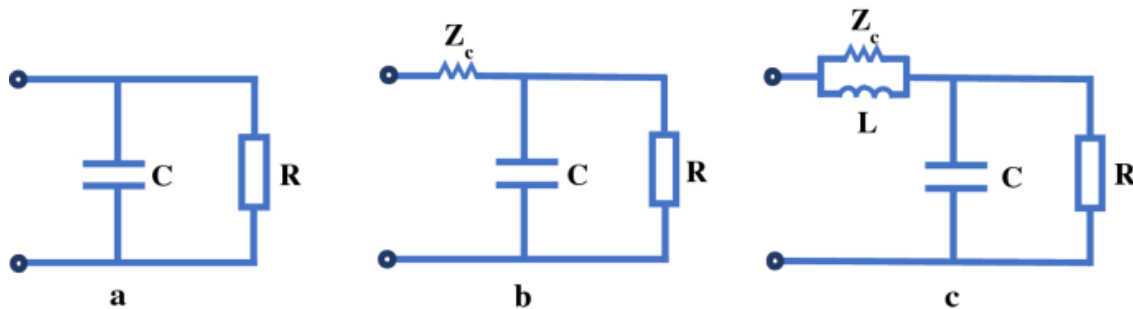


Figure 6. Windkessel models of terminal vasculature. a: 2-element Windkessel consisting of a capacitor (C) and a resistor (R). b: 3-element Windkessel consisting of an impedance (Z_c), a capacitor and a resistor. c: 4-element Windkessel consisting of an inductance (L), impedance, capacitor, and resistor. Estimating these parameters is part of patient-specific modelling. Also see Figure 20.

Recently, Duanmu et al. developed a detailed lumped parameter model for coronary hemodynamics using clinical data consisting of CT scans to provide patient-specific

geometry and MRI for inlet blood flow dynamics²⁹. They deployed structured tree outflow models to describe the outflow boundary conditions³⁰. Summarily, the Duanmu model is a sophisticated combination of individual vessel Windkessel models shown in **Figure 6**. Coronary flow is tightly coupled the hemodynamics of the heart and the aorta. In the context of this thesis, coronary flow depends on aortic pressure and flow, the cardiac contractility, heart rate, and hemodynamic properties of downstream vasculature. To simulate coronary hemodynamics, a coronary vascular model needs to be coupled to models of the heart and the arterial system, which interact with each other. This coronary vascular model should be reasonably simple but represent the physiology of the coronary circulation sufficiently.

A lumped parameter model with multiple components, is then represented by a system of ordinary differential equations (ODEs) of the form,

$$\frac{dy}{dt} = f(y, p, t) + \textit{forcing terms representing the heart}.$$

where y contains the state variables of pressures and flows in each coronary vessel segment, p contains the parameters of the model and its components, and t is time. The initial conditions are represented by

$$y_0 = y(t = 0) \qquad \text{equation (3).}$$

which is the system when $t = 0$.

A lumped parameter description of the human heart was implemented in our recent work as a component of a whole body circulation model³¹. This model is described using the following Equations 4.1-4.3. In the human heart model, time varying elastance $E(t)$, as a

function of diastolic elastance E_d , and systolic elastance E_s of each chamber is provided as:

$$E(t) = E_d + \frac{E_s - E_d}{2} \alpha(t) \quad \text{equation (4.1).}$$

where $\alpha(t)$ is the time dependant activation function, specific to each chamber. In both ventricles, the activation function is:

$$\alpha_{ventricle}(t) = \begin{cases} 1 - \cos\left(\pi \frac{t - T_{av}}{T_{s,v}}\right), & T_{av} < t \leq T_{av} + T_{s,v} \\ 1 + \cos\left(2\pi \frac{t - (T_{av} - T_{s,v})}{T_{s,v}}\right), & T_{av} + T_{s,v} < t \leq T_{av} + \frac{3}{2}T_{s,v} \end{cases} \quad \text{equation (4.2).}$$

In both atrial chambers, the activation function is:

$$\alpha_{atrium}(t) = \begin{cases} 1 - \cos\left(\pi \frac{t}{T_{s,a}}\right), & 0 < t \leq T_{s,a} \\ 1 + \cos\left(2\pi \frac{t - T_{s,a}}{T_{s,a}}\right), & T_{s,a} < t \leq \frac{3}{2}T_{s,a} \\ 0 & \end{cases} \quad \text{equation (4.3).}$$

In the above equations, the atrio-ventricular time-delay T_{av} is 0.2 s. The ventricular systolic time duration $T_{s,v}$ and atrial systolic time duration $T_{s,a}$ both are proportional to \sqrt{T} , where T is the cardiac cycle duration.

The above lumped parameter modelling equations are initial value problems that were solved using an implicit 6th-order backward-differentiation formula to obtain stable and accurate numerical solutions³².

1.3.6 One-dimensional modelling equations.

Models described using one-dimensional (1D) equations can capture relevant wave propagation phenomena along the tortuous coronary blood vessel axis. Consecutive blood vessels may subtend an angle to each other. 1D models are described using 1D Navier Stokes equations. 1D models assume radial symmetry meaning that the dominant component of blood flow velocity is along the vessel axis and that the pressure is constant over the cross-section of the vessel. Downstream from the coupled 1D vessel network, boundary conditions are described using either lumped parameter models or observational data (pressure or flow). 1D models provide significantly deeper insights compared to lumped parameter models while simultaneously being computationally tractable which makes them practical instruments of research³³⁻³⁵.

One-dimensional modelling is performed using finite elements. In brief, each vessel is described as a sequence of several finite elements. Each vessel in turn is then connected to other vessels or is a terminal. In each finite element, hemodynamics is described using the 1D Navier Stokes equations³⁶:

$$\frac{\partial \rho}{\partial t} + \frac{\partial}{\partial x}(\rho u) = 0 \quad \text{equation (5.1).}$$

$$p - p_0 = \frac{4Eh}{3r_0(x)} \left(1 - \sqrt{\frac{A}{A_0}}\right) \quad \text{equation (5.2).}$$

A. Whole body circulation model.

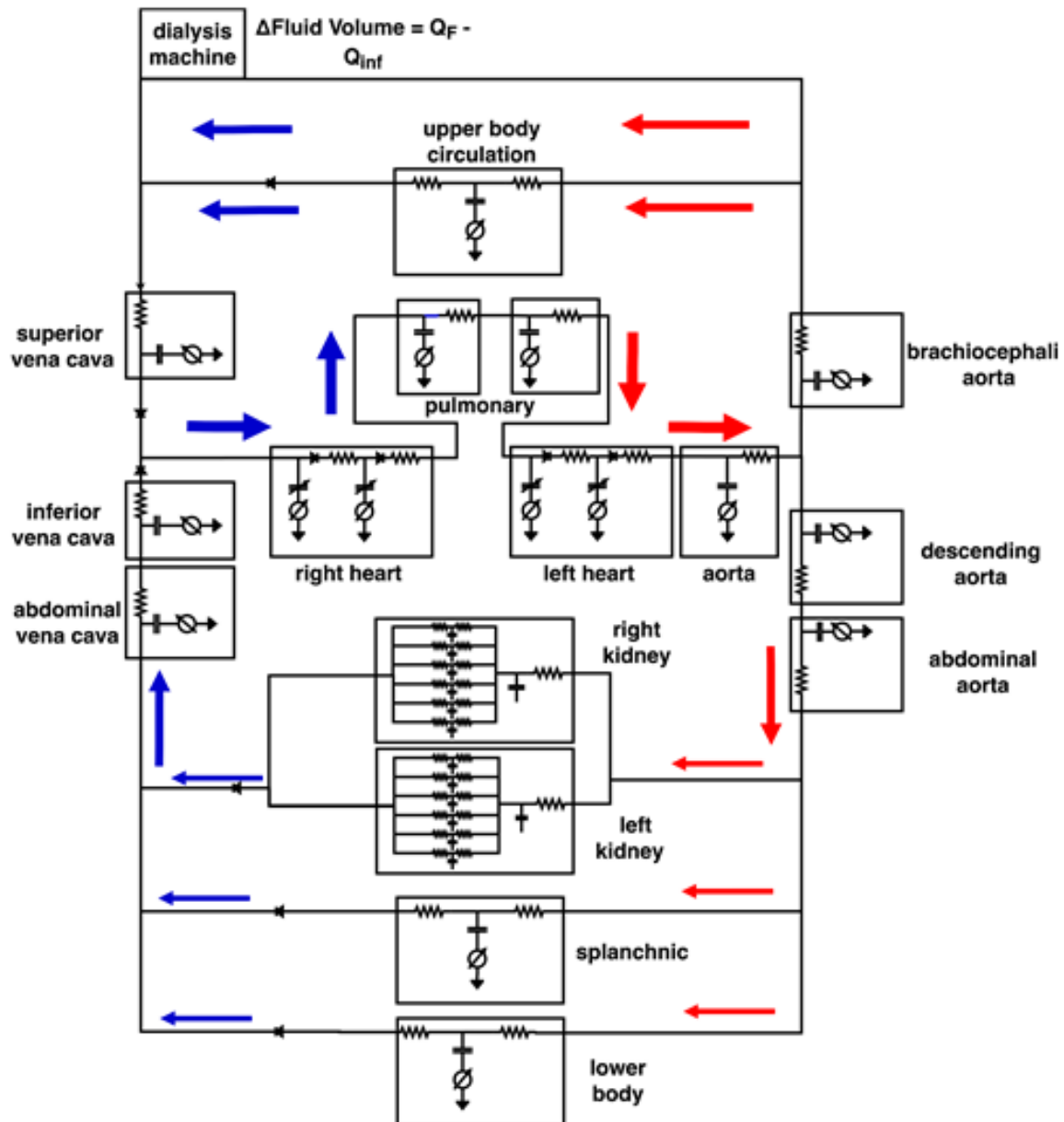


Figure 7. Diagram of whole-body circulation model used. Coronary artery models developed in this thesis were coupled to this model at the aorta and vena cava.

where ρ is the blood density, u is blood velocity along the axis of the finite element, t is time, p is pressure, and μ is blood viscosity. Using the cross-sectional area, $A(x, t)$ and the axial blood flow velocity, the actual blood flow $q(x, t)$ is computed. The above equations assume a fully developed flow profile with no slip boundary conditions at the elastic walls. Since there are three variables in the above two equations, a constitutive relationship between the blood pressure and vessel cross sectional area must be assumed:

$$p - p_0 = \frac{4Eh}{3r_0(x)} \left(1 - \sqrt{\frac{A}{A_0}}\right) \quad \text{equation (5.3).}$$

where E is the Young's modulus, p_0 is the reference pressure, A_0 is the resting cross sectional area, h is the thickness of the wall. The parameter r_0 is estimated using the following³⁰:

$$\frac{Eh}{r_0} = k_1 e^{k_2 r_0} + k_3 \quad \text{equation (6).}$$

where k_1 , k_2 , k_3 are measured experimentally to provide the stiffness at a particular location in a coronary vessel.

In the scientific platform (scientific software) used in this thesis³⁷, the above equations are encoded as 1D implicit³⁸ finite elements with suitable interpolating functions to permit generation of the spatial solution. The accuracy of this spatial solution is second order, $O(dx^2)$. The temporal solution is evolved using a second order Crank-Nickelson method

that is of second order in time, $O(dt^2)$. The time and spatial solutions are solved iteratively using an operator splitting method³⁹.

1.3.7 Three-dimensional modelling equations.

The imaging driven vascular anatomies are often used in conjunction with 3D Navier Stokes equations to gain insights into coronary blood flow. A representative 3D geometry is illustrated in **Figure 6**.

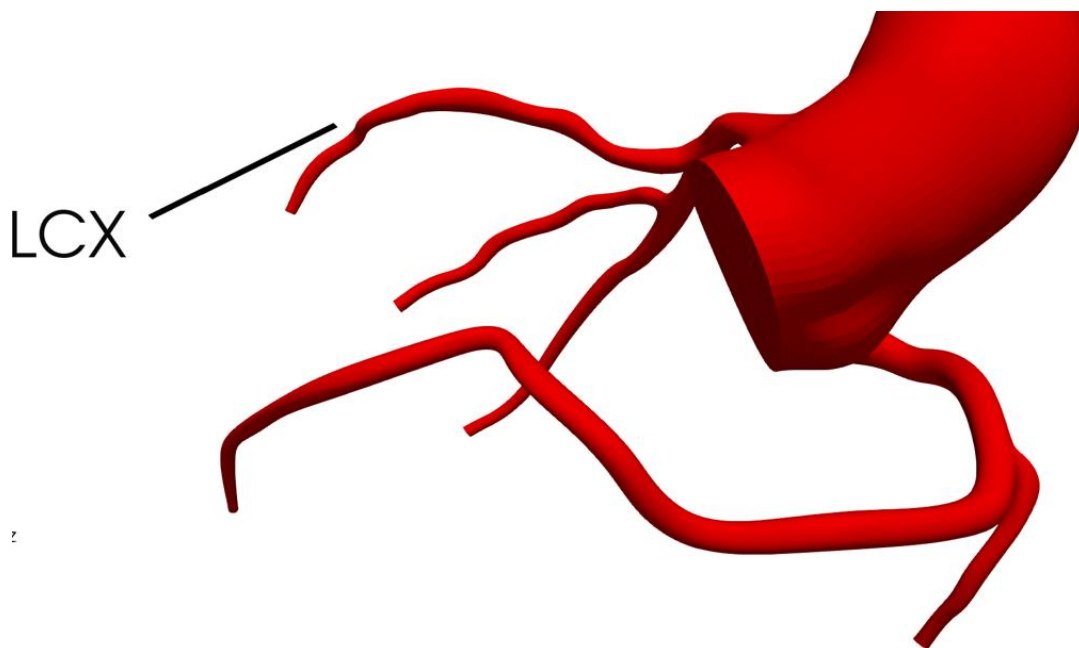


Figure 8. Representative imaging drive 3D geometry of coronary arteries and aorta. The left circumflex coronary artery (LCX) is shown.

The 3D equations governing incompressible fluid flow⁴⁰ are the continuity equation (conservation of mass):

$$\nabla \cdot v = 0, \quad \text{equation (7).}$$

and the momentum equation:

$$\frac{\partial v}{\partial t} + Re v \cdot \nabla v = -Re \nabla p + \nabla^2 v \quad \text{equation (8).}$$

where the Reynolds number, $Re = \frac{\rho \bar{v} L}{\mu}$, \bar{v} is the characteristic velocity, and L is the vessel's characteristic length.

The unknowns in the 3D equations are \mathbf{v} and \mathbf{p} which are together defined by the two equations above making the system not so well defined.

A fully developed inlet flow boundary condition is generally applied at the inlet of our hemodynamic models. To do so, flow profiles at the aortic root can be obtained from the literature⁴¹ or can be generated from our models^{42,43}.

A brief list of resources for hemodynamic modelling are provided in **Table 1**.

Table 1. A list of open-source hemodynamic simulation platforms.

Platform name.	Method.	Reference.
0D		
NSR Physiome project. Java applets.	Mechanistic ODE.	https://www.imagwiki.nibib.nih.gov/physiome
Beard et al models repository. Matlab programs.		https://virtualrat.org .
CellML XML, translated to C and Matlab using OpenCOR.		https://www.cellml.org
ModelsDB. User contributed programming paradigm.		http://www.modeldb.science
1D		
SimVascular. C++ based on Boost, Blas/Lapack, python wrappers.	Finite elements.	http://simvascular.github.io
3D		
SimVascular.	Finite elements.	http://simvascular.github.io

C++ based on Boost, Blas/Lapack, python wrappers.		
Crimson. C++ based on advanced libraries.	Finite elements.	http://www.crimson.software/publications.html
HemeLB. C++ based on advanced libraries.	Lattice Boltzmann.	http://www.hemelb.org

1.4 Thesis Hypothesis and Aims.

1.4.1 Hypothesis.

To explore factors affecting FFR, the following hypotheses were tested (chapter 2):

H1. *“presence of microvascular dysfunction (outlet boundary conditions) is a prime regulators of FFR”*; and

H2. *“diffuse stenosis (the length of vessel constriction) is more important than focal stenosis (diameter reduction) for the FFR index”*; and

H3. *“sensitivity analysis using partial rank correlation coefficient may reveal other FFR affecting factors”*.

1.4.2 Aims.

This thesis aimed to:

Aim 1. implement a dynamic coronary CFD model to explore the structure function relationships in coronary hemodynamics (chapter 2) to test above hypothesis; and

Aim 2. generate computational geometries using provided CT imaging data (chapter 3).

Chapter 2. Structure (epicardial stenosis) and function (microvascular dysfunction) that influences coronary fractional flow reserve estimation.

This chapter which addressed Aim 1 of this thesis is based upon the following article:

Joseph, J.J., Sun, C., Lee, T.-Y., Goldman, D., Kharche, S.R., McIntyre, C.W. *Structure (Epicardial Stenosis) and Function (Microvascular Dysfunction) That Influence Coronary Fractional Flow Reserve Estimation.* Appl. Sci. **2022**, 12(4281).
<https://doi.org/10.3390/app12094281>.

2.1 Abstract.

Background. The treatment of coronary stenosis relies on invasive high risk surgical assessment to generate the fractional flow reserve diagnostics index, a ratio of distal to proximal pressures in respect of coronary atherosclerotic plaque causing stenosis. Non-invasive methods are therefore a need of the times. This study proposes an extensible mathematical description of the coronary vasculature that permits rapid estimation of the coronary fractional flow reserve. *Methods.* By adapting an existing closed loop model of human coronary blood flow, the effects of large vessel stenosis and microvascular disease on fractional flow reserve were quantified. Several simulations generated flow and pressure information which was used to compute fractional flow reserve under a spectrum of conditions including focal stenosis, diffuse stenosis, and microvascular disease. Sensitivity analysis stratified the influence of model parameters on the index. The model was simulated as coupled non-linear ordinary differential equations and numerically solved using an implicit higher order method.

Results. Large vessel stenosis affected fractional flow reserve. The model predicts that the presence, rather than severity, of microvascular disease affect coronary flow deleteriously. Sensitivity analysis revealed that heart rate may not affect the index.

Conclusions. The model provides a computationally inexpensive instrument for future in silico coronary blood flow investigations as well as clinical-imaging decision making. A combination of focal and diffuse stenosis appears to be essential in reducing the index. In addition to pressure measurements in the large epicardial vessels, diagnosis of microvascular disease is essential. The independence of the index with respect to heart rate suggests that computationally inexpensive steady state simulations may provide sufficient information to reliably compute the index.

2.2 Introduction.

Clinical relevance of and potential sources of uncertainty in fractional flow reserve estimation: Coronary vessel severity of the stenosis is clinically quantified using fractional flow reserve (FFR)^{44,45}. It allows objective clinical decision making especially when computed tomography subjectively indicates intermediate coronary stenosis. Several clinical trials have promoted the clinical acceptance of FFR for quantitative diagnostics^{46,47}. FFR is clinically measured by determination of the ratio of time averaged blood flow through a stenosed vessel to that in the same vessel if it were normal⁴⁸. The imaging burden on the patient is reduced by using pressure as a surrogate to blood flow, thereby eliminating the contrast enhanced imaging requirement of the hyperemic patient. In recent times, non-invasive computed tomography angiography combined with computational fluid dynamics (CFD) has become increasing prevalent to estimate FFR, and aimed at reducing the significant risks associated with invasive pressure wire measurements⁴⁹. However, multiple complex physiological processes render uncertainty

to FFR estimation⁵⁰. Particularly, the clinical literature suggests that microvascular dysfunction and stenosis morphology play a significant role in the estimated FFR. In addition, surgical and pharmacological sensitivity remains limited where adverse events often occur in critically ill patients such as those with renal failure⁵¹ where diagnostics are sub-optimal.

A brief overview of coronary FFR modelling to date: The computed tomography angiography driven computational estimation of FFR is now an advanced technology⁵². Combining imaging with computational fluid dynamics assessment of FFR is known to increase the specificity of diagnosing lesion specific ischemia⁵³. It is facilitated by ready availability of open source advanced scientific platforms^{37,54–56} including those developed in house (Virtual Cardiac Physiology Laboratory)^{42,57}. Typically, computation of FFR combines an imaging driven generation of 3D coronary anatomical geometry with a model of coronary physiology to provide boundary conditions including cardiac output, aortic pressure, and microvascular resistance, together in which appropriate laws of fluid flow physics simulate coronary hemodynamics. The approach has been deployed to study a spectrum of processes involving FFR estimation refinement⁵⁸, interplay among multiple stenosis complexes⁵⁹, and perioperative treatment assessment⁶⁰ among several other applications. Higher order 3D computational modelling is a high performance computing application and cannot be performed onsite by the clinician. Due to data heterogeneity resulting in the need to explore parameter spaces^{61,62}, large scale computations remain unwarranted in a clinical environment. Recent studies demonstrate the applicability of lumped parameter (0D) modelling. The role of peripheral arterial disease in hypertension was addressed using a human 0D model⁴³. A detailed whole body human model tested

the effects of treatments such as hypothermia and exercise on the systemic circulation⁴². The debilitating effects of atrial fibrillation on cerebral circulation were illuminated by Hunter et al.⁶³. However, computationally efficient modelling of coronary blood flow dynamics remains limited⁶⁴. It is therefore relevant to make an open source and extensible lumped parameter model of the coronary circulation.

Study aims: In this work, an existing lumped parameter (0D) model of the coronary vasculature⁶⁵ was further developed and used to demonstrate important factors that regulate FFR. Specifically, the dependence of FFR on the nature of stenosis (focal or diffuse) and on microvascular status was investigated. Further, a PRCC based sensitivity analysis⁶⁶ was performed to stratify the impact of model parameters on FFR. For this purpose, a 0D modelling approach was found to be suitable as the study's goal was to understand coronary flow in the presence of pathological conditions. It can be appreciated that model identification (personalization), although highly desirable, was not essential in this theoretical study. As such, the presented model is theoretical in nature using which a better understanding of pathophysiological processes was prioritized over model personalization. The model has high manipulability and extensibility.

2.3 Materials and Methods.

Model development: A recent model of the coronary circulation was adapted. It consists of 16 epicardial coronary artery segments including the left anterior descending (LAD), left circumflex artery (LCX), right coronary artery (RCA), and several of their clinically significant daughter segments. The closed loop connectivity of the structured tree network is illustrated in **Figure 9** and the names of all arteries are elaborated in **Table 2**. Each artery segment is characterized by the Windkessel time independent parameters that

consist of a hydraulic resistance (R_n), the inertia to flow of blood represented by an inductance (L_n), and the elastic capacity of the vessel, C_n ²⁸.

Each artery segment entering a capillary bed leading into the venous circulation was further assumed to experience a microvasculature terminal impedance (Z_i) that was estimated using a structured tree model by Olufsen³⁰ as,

$$Z_i = \frac{8\mu\lambda((2\gamma^3)^{-(N+1)} - 1)}{\pi r_0^3 (0.5\gamma^{-3} - 1)}, \quad i = 1, \dots, 9. \quad \text{Equation (8).}$$

where $\gamma = 2^{-\frac{1}{\epsilon}}$ and ϵ represents the daughter vessel radius taper exponent, λ is the ratio of microvascular length to its diameter, and r_0 is the root vessel radius of the structured tree. N represents the number of generations for each structured tree^{28,30,67}. The lumped coronary system was further developed by incorporating a detailed four chamber heart description (**Figure 9, A**)⁶⁸. For simplicity, this model does not account for the phase altering effects of cardiac contractility on microvascular coronary flow.

Using the parameters given in **Table 2 and Table 3**, and microvascular impedances calculated using Equation 2, pressure at each node of the model (**Figure 9, B**) was computed as

$$\frac{dP_n}{dt} = \frac{Q_n - Q_0}{C_n} \quad \text{Equation (9).}$$

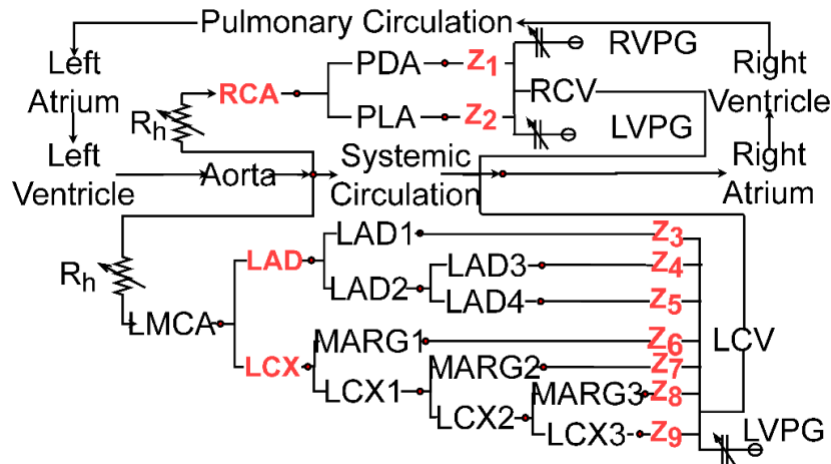
and the flow through each vessel (resistance) was calculated as

$$\frac{dQ_n}{dt} = \frac{P_{n-1} - P_n - R_n Q_n}{L_n} \quad \text{Equation (10).}$$

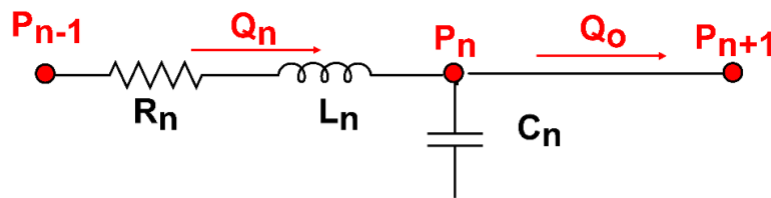
Further, the flow through each of the terminal impedances was calculated as

$$\frac{dQ_n}{dt} = \frac{P_{n-1} - P_n - R_n Q_n}{L_n} \quad \text{Equation (11).}$$

A. Model Circulation.



B. Typical vessel.



C. Legend.

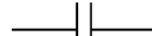
-  Vessel resistance (resistance).
-  Vessel inertia (inductance).
-  Vessel elasticity (capacitance).
-  Vessel resistance due to head loss (variable resistance).
-  Intramyocardial left and right ventricular pressure generators (LVPG & RVPG).

Figure 9. The modelled lumped parameter coronary vasculature tree network. A. Closed loop vascular structure including tree network and functional components. See Table 2 for vessel names. Z_i ($i = 1$ to 9) represent terminal vessel impedances. Vessels as well as impedances shown in red were used in the simulation

experiments. B. Typical blood vessel represented by a resistance (R_n), inductance (L_n), and a capacitance (C_n). P_{n-1} : vessel inlet pressure; Q_n : flow through vessel; P_n : pressure in vessel; Q_o : outlet flow; P_{n+1} : outlet pressure, or pressure in distal vessel. C. Symbols used in panels A, B, and elsewhere in this thesis.

Simulation experiments: In all simulations, fractional flow reserve (FFR) was computed as the average of the ratio of the time dependent distal pressure, P_d (pressure downstream from stenosis) to the time dependent proximal (aortic) pressure, P_a ,

$$FFR_{vessel} = \frac{1}{M} \sum_{n=1}^{n=M} \frac{P_{vessel,n}}{P_{aorta,n}} \quad \text{Equation (12).}$$

where M represents the total number of fractions over a given time T. Simulations were designed to explore the effects of stenosis severity in the largest epicardial vessels (either LAD, LCX, or RCA, see **Figure 9**) or microvascular disease, or both. A sensitivity analysis was performed as described below.

Stenosis in three large vessels, namely the left anterior descending artery (LAD), the left circumflex artery (LCX), and the right coronary artery (RCA), was investigated. Simulations were performed by imposing focal or diffuse stenosis in a given large vessel. To simulate focal stenosis, the blood vessel was divided into two and its biophysical parameters (**Table 2**) were revised using

$$R_s = R_0 \alpha^{-2}$$

$$C_s = C_0 \alpha^{\frac{3}{2}}$$

Equation (13).

$$L_s = L_0 \alpha^{-1}$$

where the stenosis severity, a , is given by the parameter

$$\alpha = \frac{A_s}{A_0}$$

Equation (14).

which is always between 0 and 1 by definition. A_s and A_0 are the area of the stenosed blood vessel and area of same blood vessel when healthy, respectfully.

To simulate diffuse stenosis extended through a certain length percentage x_s ($0 \leq x_s \leq 1$) of a vessel, the revised parameters were calculated as

$$R = R_s x_s + R_0 (1 - x_s)$$

$$C = C_x x_s + C_0 (1 - x_s)$$

Equation (15).

$$L = L_x x_s + L_0 (1 - x_s)$$

and used in Equations 8-10.

Microvascular disease was simulated by decreasing the terminal vessel radius by a predefined amount in all terminals. In this model, radius regulated microvascular impedance was increased by decreasing the ϵ in Equation 2's γ parameter.

Sensitivity analysis: Sensitivity of multiple model parameters including stenosis lengths, focal stenosis severity, heart rate, terminal vessel impedances, microvascular vessel taper parameter (ϵ), and number of downstream vasculature generations to FFR was computed. To do so, we used our implementation of partial ranked correlation coefficients

(PRCC)^{42,69}. The coefficients were used to rank the parameters in descending order of significance, and the most relevant results reported.

Numerical methods: The model is a system of 36 coupled stiff ordinary differential equations. Pressures and flows were computed as state variables according to governing ordinary differential equations, Equations 2 to 4 for each vessel. The system was solved using our robust implicit solver available in our simulation software^{43,70}. The method used in the solver is based on implicit backward difference formulae that provides $O(dt^6)$ accuracy. A maximum user time step of 0.005 s gave stable solutions which remained unaffected when the maximum time step was halved and doubled. Each instance generated 500 s of simulated dynamics from which the final 10 s of activity were used to generate results. Simulations were performed on local and national clusters. Each instance of the model is a serial run that took 15 seconds. To construct results in the presented work, a large number of model instances (10^6) for predefined values of physiologically relevant parameters were executed within 4 hours using 48 processors. The trivially parallel simulations were performed using GNU Utilities. The simulation outputs were post-processed using a combination of UNIX and MATLAB scripts.

Table 2. Model parameter values. See Figure 9 for vessel connectivity. The rows are color coded to suggest the major epicardial coronaries, either LAD, LCX, or RCA.

Vessel name	R (mmHg-s/ml)	C (ml/mmHg x 10⁻³)	L (mmHg-s²/ml)
LMCA	0.2299	2.9	0.00228
LAD	0.4662	1.6	0.0298
LAD1	0.5729	1.6	0.0342
LAD2	1.7077	3.4	0.0916
LAD3	3.7484	1.3	0.1115
LAD4	3.2930	0.4	0.0716
LCX	0.3929	1.2	0.0241
LCX1	0.4730	0.7	0.0231
LCX2	1.0264	0.7	0.0380
LCX3	3.2342	1.1	0.0944
MARG1	1.7351	1.2	0.0655
MARG2	2.9195	0.8	0.0787
MARG3	3.0683	1	0.0896
RCA	1.8302	6.3	0.1171
PLA	2.4412	1.1	0.0799
PDA	1.2571	1.8	0.0596

Table 3. Parameters used to compute microvascular impedances.

Z	Root vessel radius, r_0 (mm).	N.	Control Z values (mmHg-s/ml).	
Z ₁	PDA	0.108	19	134.100
Z ₂	PLA	0.130	20	083.710
Z ₃	LAD1	0.146	20	059.095
Z ₄	LAD3	0.103	19	154.592
Z ₅	LAD4	0.088	18	227.185
Z ₆	MARG1	0.116	19	108.224
Z ₇	MARG2	0.098	19	179.482
Z ₈	MARG3	0.102	19	159.184
Z ₉	LCX3	0.102	19	159.184

Legend. Z: terminal impedance; N: number of generations in microvasculature.

2.4 Results.

Model FFR during the cardiac cycle: Time dependent FFR in the three major coronary arteries (LAD, LCX, and RCA) under predefined large vessel stenosis and microvascular disease is illustrated in **Figure 10**. The control simulation (**Figure 10, top row**) devoid of stenosis or microvascular disease shows that FFR is high (more than 0.8) during the complete cardiac cycle in all three vessels. Due to flow distribution from the aorta to the smaller coronary network, the time dependent FFR was seen to reduce during systole. The time dependent FFR when either LAD, LCX, or RCA were focally stenosed by 90% is shown in **Figure 10, middle row**. When there was a full vessel length stenosis the FFR values reduced to 0.56 for the LAD, 0.52 for the LCX, and 0.5 for the RCA. Whereas the

overall FFR was observed to reduce significantly in all three simulations, large vessel stenosis led to minimal FFR during the cardiac cycle's diastole. Simulated microvascular disease, simulated by augmenting all terminal impedances by 50% ($\epsilon = 2.55$, a reduction of ϵ increases impedance, Z), led to amplifying the difference between the aortic and respective distal pressures and gave a minimal FFR estimate during the systole (**Figure 10, bottom row**). When microvascular disease was simulated the maximum time dependent FFR value was calculated to be 1 and minimum to be 0.7 in all three blood vessels.

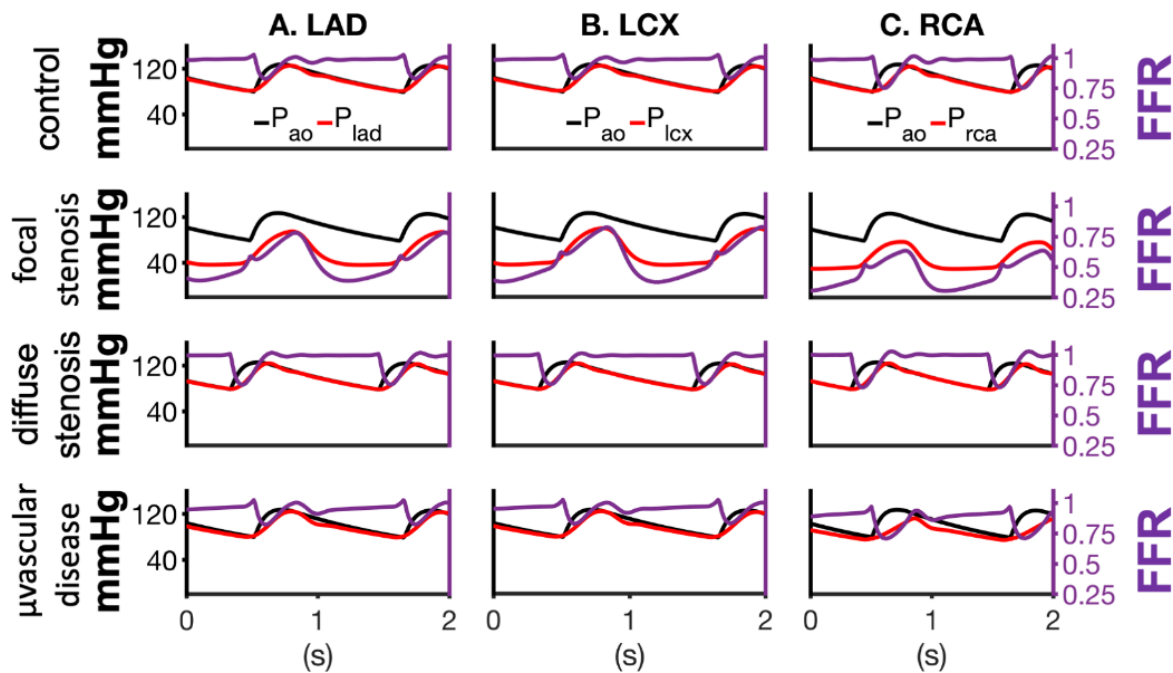


Figure 10: Pressure profiles and FFR in the LAD (column A), LCX (column B), and RCA (column C). In all columns, top row shows non stenosed model behavior, second row shows the result of focal stenosis ($\alpha = 90\%$), and third row shows the result of downstream microvascular disease in the absence of focal stenosis ($\alpha = 100\%$; $\epsilon = 2.33$). In all panels, black lines and axis represent aortic pressure

(proximal pressure) while red lines and axis represent the pressure of vessel of interest (distal pressure). Time dependent FFR is shown as orange dashed lines.

The coronary flow in the control coronary model (**Figure 11, top row**) and its reduction due to focal stenosis (**Figure 11, middle row**), and microvascular disease (**Figure 11, bottom row**) was computed. Relative to the control case (**Figure 11, top row**), focal stenosis (**Figure 11, second row**) restricted flow significantly in all 3 blood vessels. When microvascular disease was implemented, the maximum flow and overall flow in the network decreased. Further, the impact of individual artery resistances, inertances, and compliances were blunted as reflected in the flow profiles (**Figure 11, bottom row**).

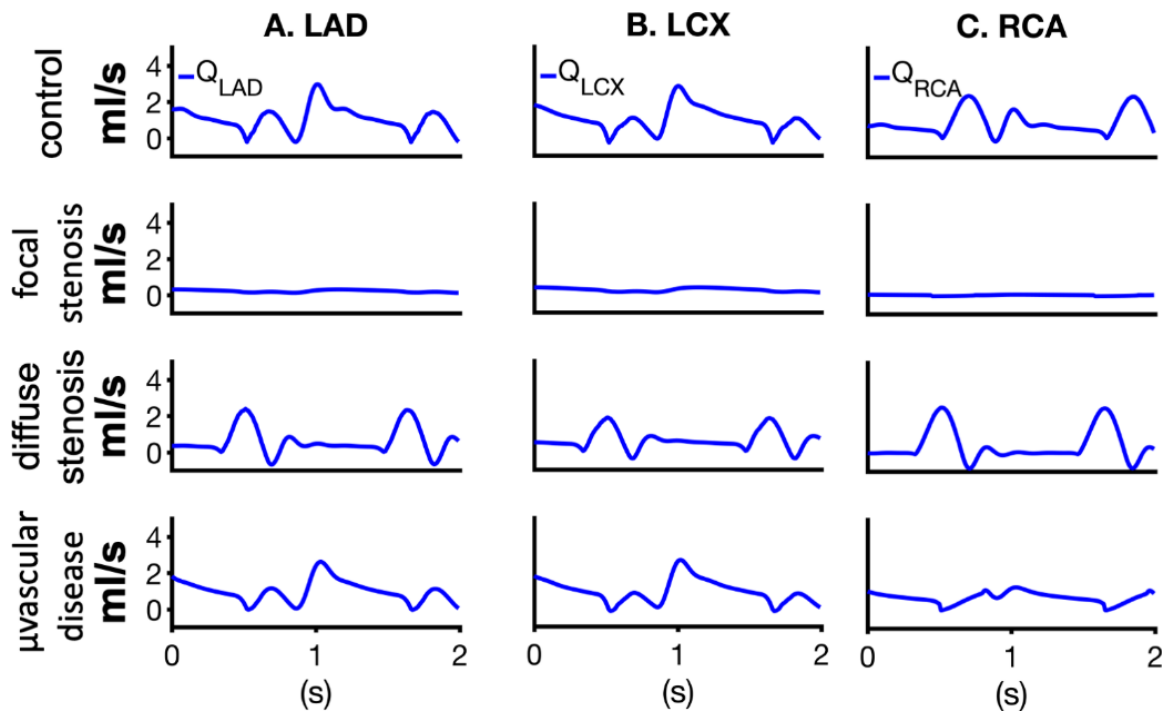


Figure 11. Flow profiles in the LAD (column A), LCX (column B), and RCA (column C). In all columns, top row shows non-stenosed (control) model flow, second row

shows flow under focal stenosis ($\alpha = 90\%$) and the third row shows the flow under microvascular disease in the absence of focal stenosis ($\alpha = 100\%$; $\epsilon = 2.33$).

Focal and diffuse stenosis interplay: The dependence of average flow (flow), maximum flow, and FFR on simultaneous presence of reduced vessel diameters (focal stenosis) and diffuse stenosis (reduction of diameters along a predefined length) were quantified (**Figure 12**). In all vessels, the detrimental effects of stenosis on flow (**Figure 12, top row**) and maximum flow (**Figure 12, middle row**) were impacted by the severity of focal stenosis (horizontal axis) to a greater extent than the severity of diffuse stenosis (vertical axis). Progressive focal stenosis alone was found to minimally impact the estimated FFR (**Figure 12, bottom row**) due to the model formulation (see above). As such, a reduction of FFR was observed when the stenosis was diffuse to a certain extent. Conversely, diffuse stenosis in the absence of focal stenosis (vertical axis in **Figure 12**) also did not reduce FFR. Progressive focal stenosis in the RCA caused the largest reduction of FFR (**Figure 12, third row**) as compared to focal stenosis in the LAD and LCX in the presented model. In the presented model, the RCA was more susceptible to FFR reduction due to stenosis in comparison to the LAD and LCX. Simultaneous presence of focal and diffuse stenosis caused the most severe reduction of FFR in the RCA, followed by in the LAD and LCX.

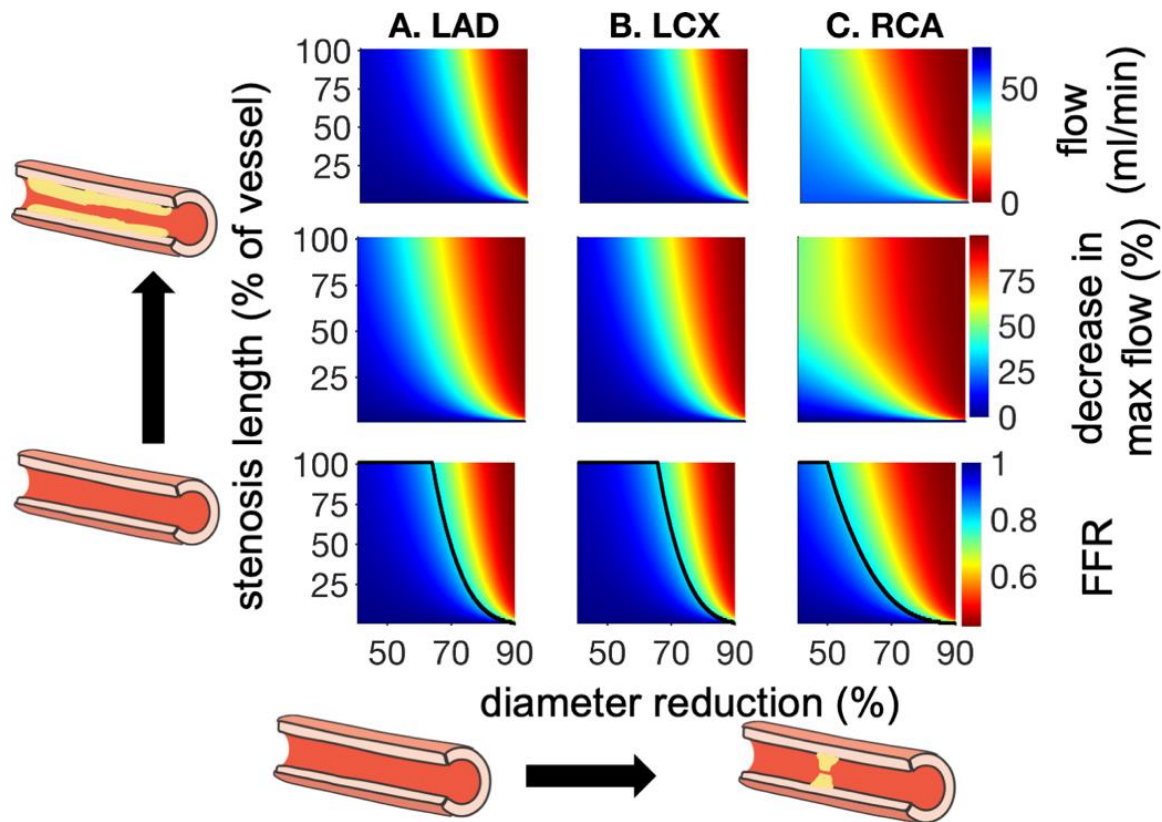


Figure 12. Dependence of flow rate (top row), maximum flow (middle row), and mean FFR (bottom row) on stenosis length (vertical axis, all panels) and vessel diameter (horizontal axis, all panels). Columns A, B, and C show LAD, LCX, and RCA results respectively. The black line in the bottom row demarcates the FFR = 0.8 threshold.

Role of microvascular disease in the modelled FFR: The average flow (flow), maximum flow, and FFR values of simultaneous focal stenosis and microvascular disease are shown in **Figure 13**. Microvascular disease was simulated by varying the daughter vessel's radius taper exponent ϵ (**Equation 8**) from 2.76 (0% microvascular disease, control) to 2.33 (100% microvascular disease)⁷¹. At diameter reductions below 70%, the flow in each blood vessel (**Figure 13, top row**) is significantly restricted by up to half of

the control flow with the increase in severity of microvascular disease. At similar diameter reductions in the LAD and LCX however, the peak reduction in max flow values (near 0.5 of the control values) occur at 50% microvascular disease and returns to near control values at maximal microvascular disease. At diameter reductions above 80%, microvascular exacerbates the effect of the stenosis on FFR values. However, an almost unique value of diameter reduction for each, LAD, LCX, and RCA, was observed to characterize a clinically significant FFR transition to below 0.8 in the presence of an arbitrary severity microvascular disease. While the diameter reduction was 0.7 for LAD and LCX, it was seen to be a much lower 0.55 in case of the RCA.

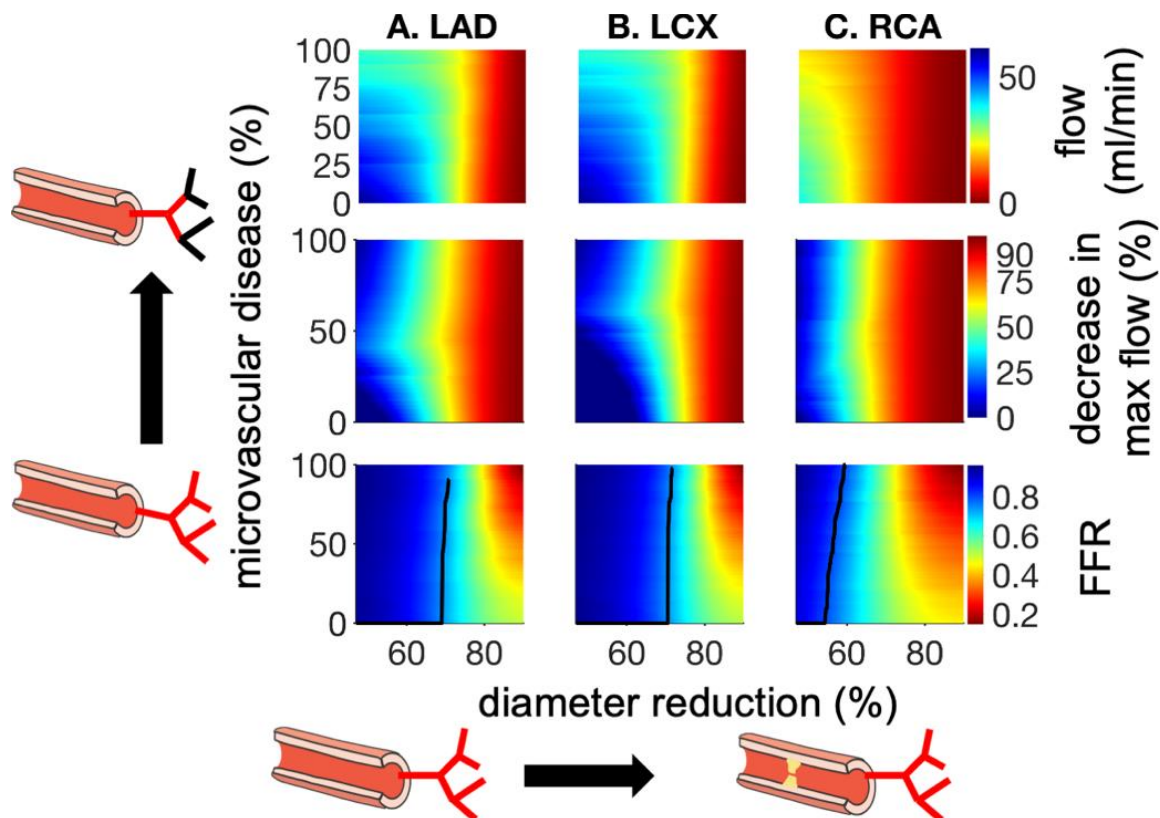


Figure 13. Dependence of flow rate (top row), maximum flow (middle row), and mean FFR (bottom row) on microvascular resistance increase (microvascular

disease, vertical axis in all panels) and vessel diameter (horizontal axis, all panels). Columns A, B, and C show LAD, LCX, and RCA results respectively. The black line in the bottom row demarcates the FFR = 0.8 threshold.

Sensitivity analysis to stratify FFR impacting parameters: The results of the sensitivity analysis are shown in **Figure 14** and **Figure 15**. The histograms of FFR values obtained during the PRCC calculation are shown in **Figure 14**. As can be seen, the model did not produce any instances with FFR less than 0.3 due to the ranges of parameters considered. The model appears to produce FFR values centered around 0.54. Further, in all 3 coronaries the FFR values appear to be distributed in a left skewed Gaussian manner.

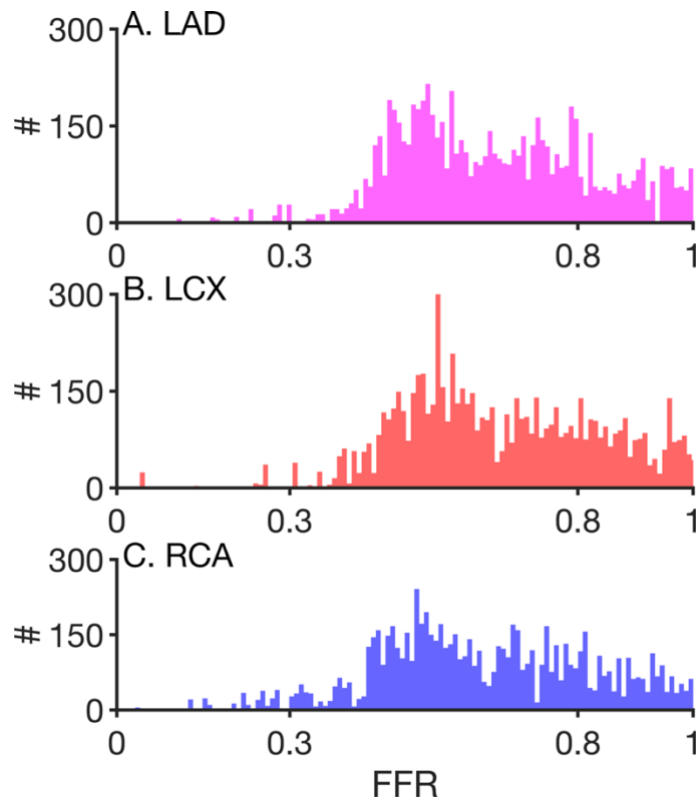


Figure 14. Histograms of FFR obtained from PRCC simulations (see Figure 7). Panel A shows the data for LAD, panel B for LCX, and panel C for RCA.

The sensitivity analysis generated PRCC coefficients are shown in **Figure 15**. The heart rate (HR) is the most impactful model parameter regulating the FFR. Consistently, focal stenosis (fs) is also a significant regulator of PRCC. Both HR and fs negatively regulate FFR. Diffuse stenosis (ds) and the right ventricular systolic elastance ($E_{\text{sys},rv}$) also negatively regulate FFR. The microvascular parameters (microvascular root radius r_0 , and tapering factor ε) also affect FFR according to our sensitivity analysis.

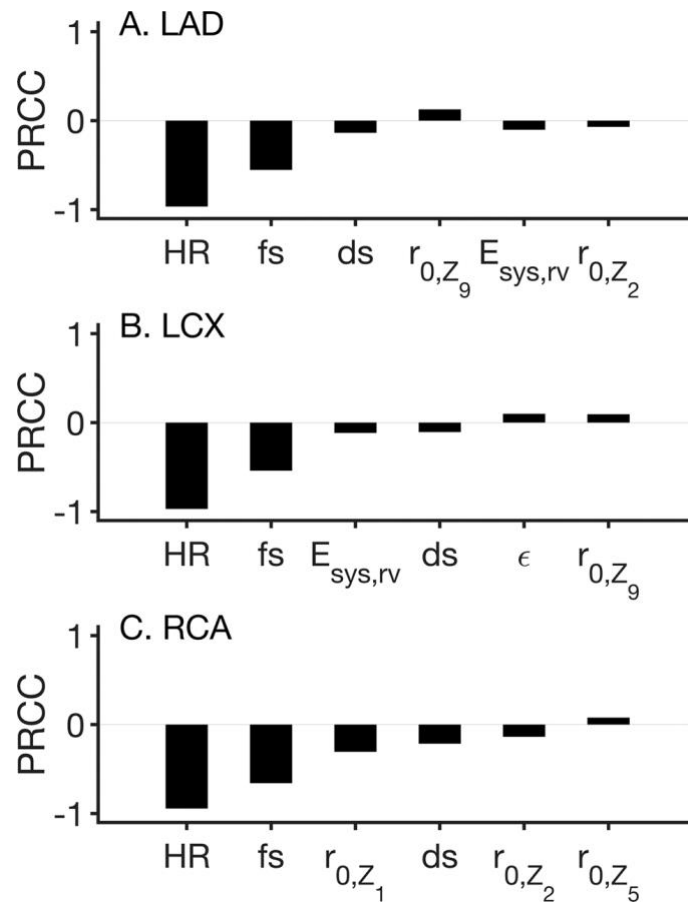


Figure 15. PRCC sensitivity of FFR to model control parameters. In all panels, the sensitivity of FFR to the six most relevant parameters are shown. Panel A shows the PRCC for LAD, panel B for the LCX, and panel C for the RCA. In all panels, HR: heart rate; fs: focal stenosis; ds: diffuse stenosis; r_0 : root radius of microvascular bed; Z_i : microvascular impedance; ϵ : microvasculature taper exponent; and $E_{sys,rv}$: systolic elastance of the right ventricle.

2.5 Limitations and Future Directions.

Further development of the presented model will lead to its clinical applicability. Whereas a detailed heart model^{72,73} was incorporated into the lumped parameter description⁶⁵, the simulated aortic root inflow to the coronary vasculature remains generic. Upon availability,

patient specific aortic root blood flow profiles will alleviate the limitation. In a similar manner, the vessel parameters and microvascular impedances were summarized from the literature^{28,65}. Patient specific model identification will increase the applicability of the model and reduce its prediction uncertainty. The inclusion of vessel specific biomechanical properties and inclusion of a reactive vascular tone module^{69,74,75} is expected to allow simulation of clinical parameters such as pulse wave velocities and residence times^{76–80}. The inclusion of autoregulatory processes will further assist to make the model's FFR estimates quantitatively reliable⁸¹.

Although the model is theoretical in nature, the presented results will guide our future work. As such, the findings of the study remain informative for deeper lumped parameter modelling and will inform our spatially extended modelling.

2.6 Conclusions and Discussion.

Focal and diffuse coronary stenosis were both observed to modulate FFR (**Figure 12**). As our results indicate, the diffuse nature of stenosis may reduce coronary blood flow greater than diameter reduction alone (thesis hypothesis H2). However, our simulations indicate that FFR estimation must consider other conditions such as microvascular disease, both of which are routinely diagnosed among patients using non-invasive techniques. Furthermore, it appears that blood flow to the right ventricle is more severely affected due to the extra-coronary and RCA stenosis conditions (**Figure 12** and **Figure 13**). Novel imaging protocols that account for cardiac chamber to chamber diastole will fortify further refinement of the diagnostic instrument.

As seen in **Figure 12**, focal as well as diffuse stenosis reduces FFR relative to the control case. However, it can also be seen that extra-coronary conditions such as microvascular disease also affect FFR estimates (thesis hypothesis H1). It is therefore clear that

consideration of the effects of co-morbidities is essential in FFR estimation. The result also indicates that our approach is suitable for ranking the severity of co-morbidities. Specially, **Figure 11**, indicates that microvascular disease alone does affect FFR estimation (see definition of FFR). Furthermore, the left and right heart's coronary are affected differentially. Whereas imaging studies are optimized to provide information regarding left coronaries, the model suggests that the right coronaries should also be considered. Our model suggests that stenosis may not be an exclusive focal or diffuse phenomenon. As **Figure 12** shows, consideration of a combination of the two natures of stenosis is essential, especially in our future higher dimensional modelling. In future studies, the 0D models in this detailed investigation will be useful as boundary conditions to 3D model computational fluid dynamics⁸². In addition to detailed geometry, **Figure 12** indicates that a priori knowledge of microvascular health status will permit 3D models to provide better FFR estimates. Within the confines of the presented model, the sensitivity analysis (**Figure 15**) suggests that heart function such as heart rate and systolic heart elastances are also regulators of FFR (thesis hypothesis H3).

Data availability. The codes to reproduce results of Chapter 2 are available from:

https://github.com/mccsssk2/HumanCirculationModel2022_MDPI

Chapter 3. Image processing to generate computational coronary geometries.

3.1 Description of coronary CT data from the Lee lab.

Coronary CT imaging data was obtained from Prof. Ting-Yim Lee's laboratory⁸³ (<https://www.lawsonimaging.ca/imaging/user/19>) to generate ten computational geometries (**Figure 16**). The Lee lab are specialists in clinical imaging with a vision to reduce radiation exposure while improving image quality. For the purposes of this study, ten swine coronary CT image stacks were obtained. The Lee lab acquired the data between 2016 and 2020. The data were acquired on the CT scanners in St. Joseph's Hospital, London, Ontario. The CT scanners have a bore size of 72 cm, a coverage of 4 cm, use 80kW of power, and have a rotation speed of up to 0.35 sec. The CT images are in DICOM format. Each of the 2D images are stored as 512 (x) X 512 (y) pixel files. The data are stored as 16-bit grayscale. The in plane resolution of the 2D images is 0.4883 mm (x) X 0.4883 mm (y). The inter slice distance is 0.625 mm. The data are stored by the Lee lab in their large storage which were made available for this study upon reasonable request. The data were thoroughly anonymized for patient information, referring physician identity, operator identity, and all other sensitive identity information. Representative slices from the data are shown in **Figure 17**. These are the images that were segmented to generate computational geometries.

3.2 Semi-automatic segmentation.

Modelling technology to generate solid models from imaging has developed previously⁸⁴. This has motivated the intention of creating software and tools for better visualization and

operations to be performed. In this thesis, a tool called the Visualization Tool Kit (VTK) was combined with a imaging to model pipeline called SimVascular to develop the geometric models³⁷. The process is pictorially summarized in **Figure 16**.

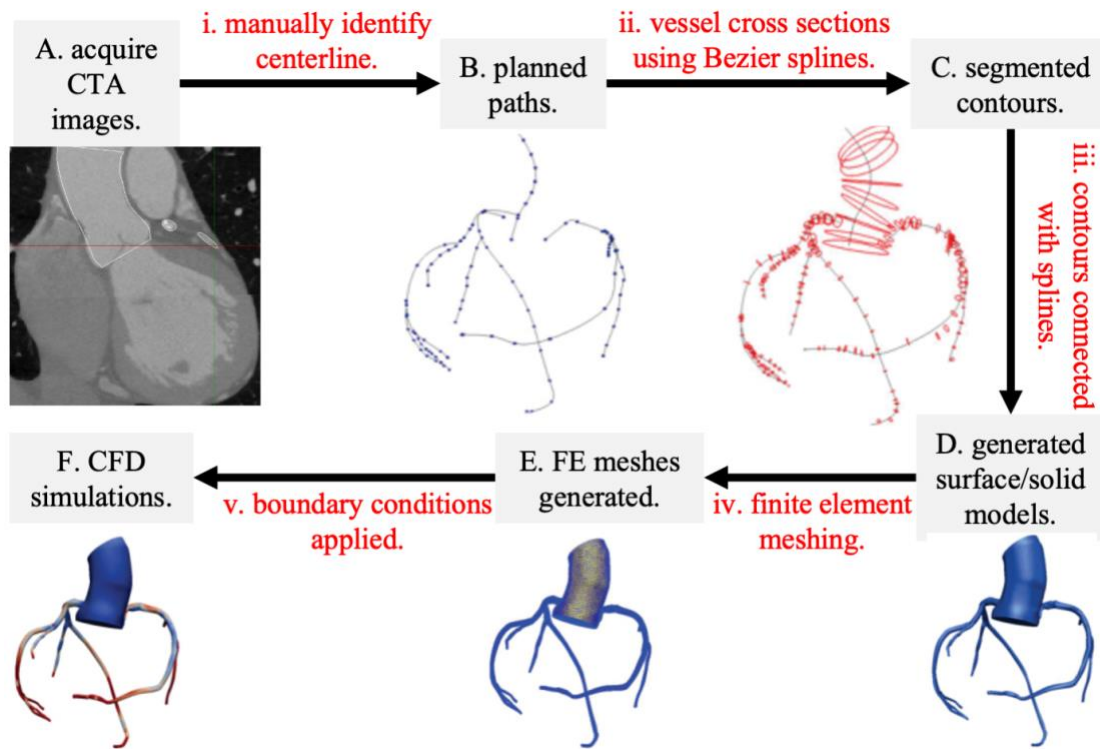


Figure 16. Summary of pipeline to generate geometries. CT image visualization: the images are visualized using scientific visualization software MITK-VTK, which provides the basis for semi-automatic user segmentation. **Path planning:** the platform generates a smooth vessel path based on user provided fiducial points. **Segmentation:** the user draws circles around cross sections using fiducial points along each vessel. **Solid modelling:** the paths and segmentations are combined to generate vessel surfaces and volumes. **Meshing:** the surfaces and volumes are both meshed as finite element meshes. **Simulation:** after applying appropriate boundary conditions, blood flow in the model is simulated.

The pipeline followed in this thesis to generate the 3D models for simulation begin with computerized tomography (CT) images of the thoracic region of the body. These image stacks are imported into a graphical software (**Figure 16, A**) and a volume visualization is rendered to identify the anatomy of the coronary vasculature. Once arteries are identified, each of their centrelines is obtained by user defined fiducial points (**Figure 16, i**) and functions built in the software (**Figure 16, B**). Using these features, the vessels were segmented and geometric models generated. The reconstructed models provide the necessary geometric properties to construct a finite element mesh that can then be used to conduct hemodynamic simulations.

The process of creating geometric models of the coronary vasculature from CT images involves the use of multiple software. The main application used in this process is SimVascular³⁷ which provides the necessary tools to graphically visualize each step of the pipeline.

3.2.1 Imaging Visualization.

The datasets used in this thesis are a set of data format for CT images specified by the Digital Imaging and Communications in Medicine (DICOM) standard stacks⁸⁵. The images are taken through the axial plane of the subject and covers most of the thoracic region. A brief sequence of images from a representative dataset are shown in **Figure 17**.

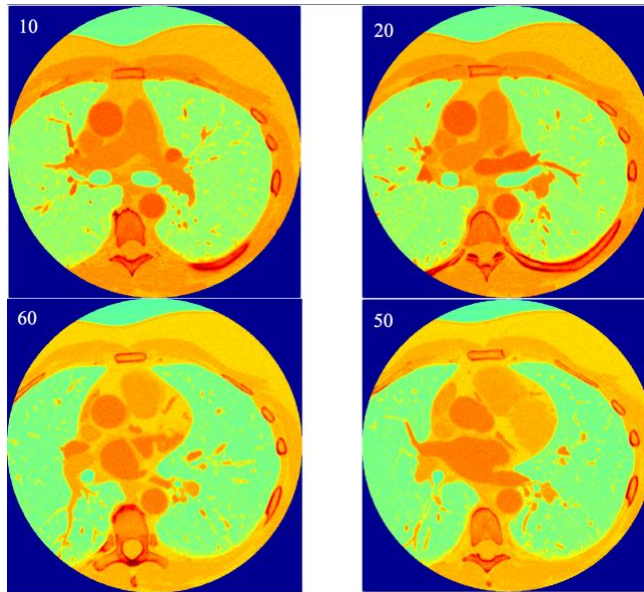


Figure 17. Representative slices from the axial planes from an imaging dataset. Numbers in the top right corner correspond to the slice number from our dataset. The 16-bit grayscale images were visualized using an appropriate color mapping scheme for the reader. All slices show the myocardial walls, the spine, the abdominal cavity, as well as the coronary vessels.

3.2.2 Extracting of center lines from CT data.

With the images and different plane views (axial, sagittal, coronal), the paths of the center lines of each vessel of interest needs to be obtained. The paths to be created determine where the segmentations will be performed. It is important that the path covers the distance of the entire vessel of interest and vessel paths intersect if they are connected. The paths are generated by using control (also called user defined fiducial points) and path points **Figure 18**.

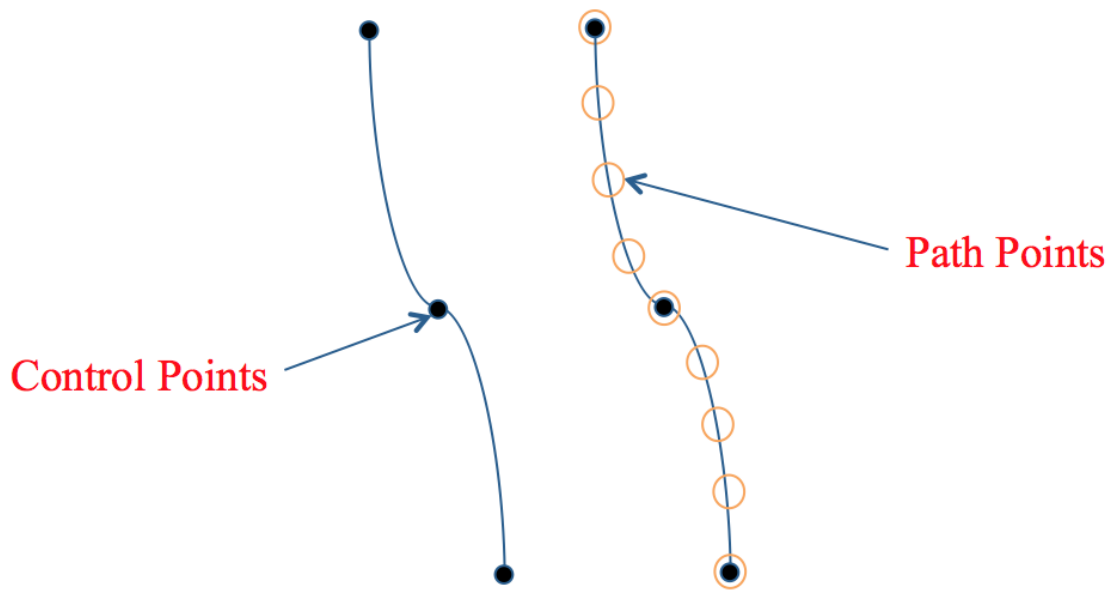


Figure 18. Control points (user defined fiducial points) of the vessel and path points. The user defines control points (left) of the vessel centrelines by visual inspection. The segmentation software provides path points (right) using algorithms based on Bezier curve fitting.

Control points are the ordered set of points the user has to indicate whereas path points are the vessel centreline locations obtained using spline based calculations.

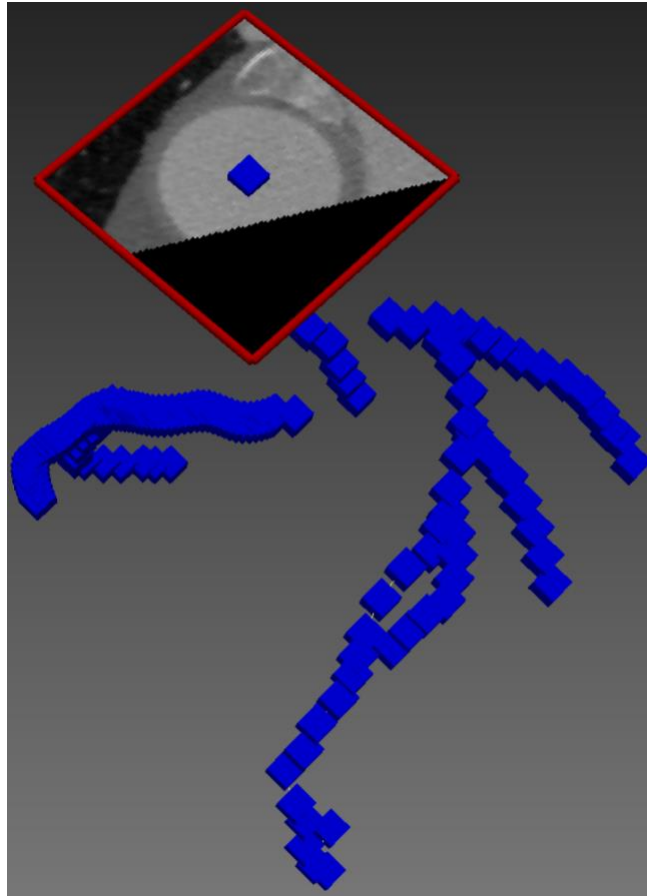


Figure 19. Path points obtained from a dataset. The inset shows one control point identified by the user. The software extends these control points to generate multiple path points shown in the main figure that track individual blood vessels.

3.2.3 Blood vessel lumen segmentation.

The goal of image segmentation is to identify 2D structures or objects. In this thesis, segmentation's purpose is to find the vessel lumens using the paths previously obtained. For all model segmentation, the process was performed twice to ensure sufficient accuracy and detail from the imaging to model pipeline.

An example of the segmentations obtained for an aorta is shown in **Figure 20**.

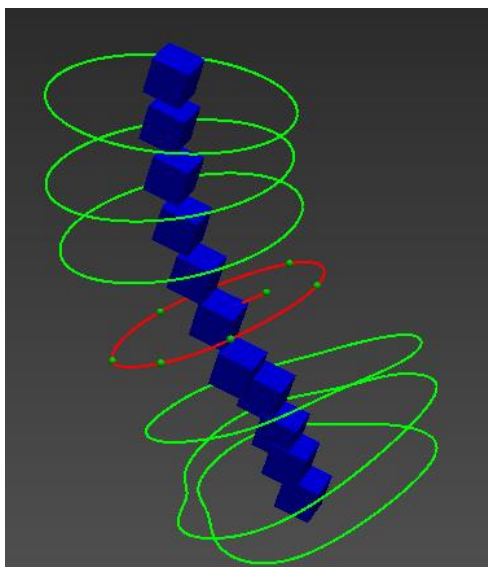


Figure 20. Example aorta segmentation. The blue points represent the determined path points along the vessel. The user drawn segmentations are shown as green closed contours. A generic contour with the user defined fiducial points in shown in red.

The path is used to help generate perpendicular plane that is used to create the lumen segmentation. **Figure 20** shows a generic segmentation using the perpendicular plane to the path. While this can be done manually, this process is also semi-automated through the help of threshold methods and automated machine learning methods. The 3D level set method was used to help generate segmentation surfaces for the coronary arteries often as they were difficult to segment using the standard approach. The level set method is a mathematical framework used to represent implicit deformable surfaces described by a 3D image volume, the level set function, evolving in time. The geometry of the segmentation surface is defined by the zero is level of the level set function. The final

surface will be located at the regions corresponding to the steepest change (gradient magnitude) of image intensity.

The path is used to help generate perpendicular plane that is used to create the lumen segmentation. Figure 21 shows a segmentation using the perpendicular plane to the path.

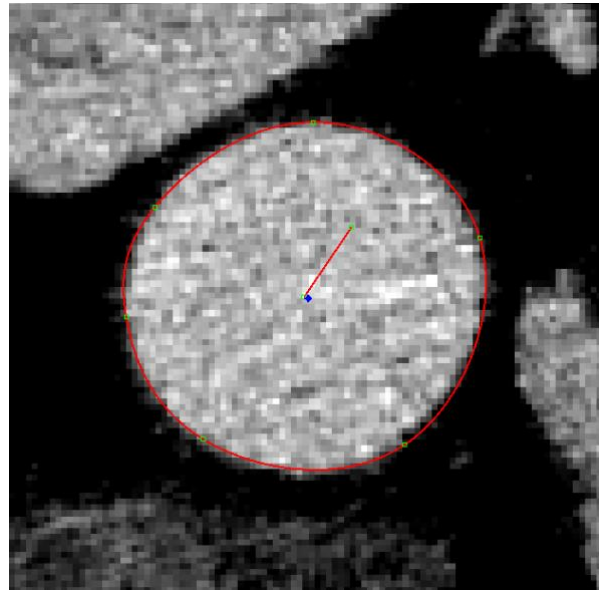


Figure 21. Segmentation of a DICOM image. In CT imaging, the contrast agents in the blood gives a signal that shows up in each DICOM image. The signal can be used to identify vessel lumen and its surface as indicated by the closed red contour. The red contour is generated by the software using the user provided fiducial points shown in green. The red contour in this figure corresponds to the red contour in Figure 20.

While this can be done manually, this process is also semi-automated through the help of threshold methods and automated machine learning methods. The 3D level set method was used to help generate segmentation surfaces for the coronary arteries often as they

were difficult to segment using the standard approach. The level set method is a mathematical framework used to represent implicit deformable surfaces described by a 3D image volume, the level set function, evolving in time. The geometry of the segmentation surface is defined by the zero iso level of the level set function. The final surface will be located at the regions corresponding to the steepest change (gradient magnitude) of image intensity.

3.2.4 Construction of 1D geometries using tracked center lines and segmented blood vessel lumens.

The 1D structure is based on a set of nodes representing the vessels of interest. An example of the programmed SWC files used in this thesis is:

1	3	100.0	100.0	100.0	1.24	-1
2	3	110.0	100.0	100.0	1.24	1
3	3	125.0	110.0	105.0	1.27	2
4	3	125.0	90.0	106.6	1.24	2
5	3	130.0	115.0	100.0	1.00	3
6	3	150.0	120.0	105.0	0.90	3
7	3	130.0	95.0	107.5	1.10	4
8	3	140.0	100.0	95.0	1.07	4
9	3	140.0	115.0	100.0	0.90	5

The first column represents the node number. In the SWC standard, the numbering starts from 1 and ends at the last node n. This numbering may need to be modified to go from 0 to n-1 when generating PM3SV scripts and use in languages such as Python (v3.6). In the SWC standard, all distances are presented in CGS units. The second column is a material property that was not used in this thesis. The third column is the x coordinate of the node (cm), while the fourth and fifth column are the y and z column of the node,

respectively. The sixth column is the radius at the node. The seventh column is the parent node number. Each node has exactly one parent. A node either has one daughter, 2 daughters, or no daughters. When a node has no daughters, it is a terminal in the geometry. For example, node 9 is a terminal in the above SWC. In particular, the parent of the starting node, also called the root node, is assigned a standardized value of -1. The example SWC file was used to generate an arbitrary geometry, and the geometry was used to perform a simple representative simulation (see **Figure 22**). The SWC file can be extended to incorporate information such as multiple parents, bifurcation angles, and metrics such as distance of node from special locations such as aortic root.

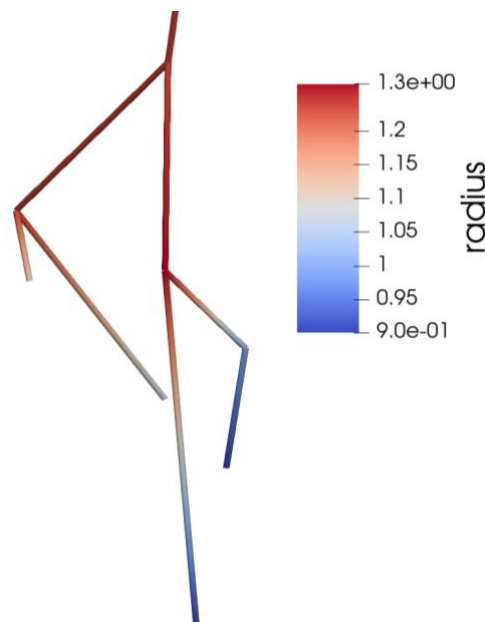


Figure 22. 1D geometry constructed using the example SWC data given on the previous page. Individual vessels are color coded using radius (cm).

3.3 3D Finite element meshing.

The reliability and accuracy of fluid simulation is a strong function of high quality meshes. It is important to produce high quality meshes but to have acceptable accuracy, the mesh resolution would have excessive computational demands. Moreover, many physical problems of interest, especially in the field of fluid mechanics, involve directional solution features, for example, boundary layers which form near the walls in viscous flows or shock waves in high-speed flows.

In this thesis, the models created from segmentations are used to discretization using finite elements. The vascular walls of the blood vessels were discretized using triangular elements. The intra-vascular lumen was discretized using tetrahedral elements. The implementation of this meshing follows from work done by Sahni et al⁸⁶.

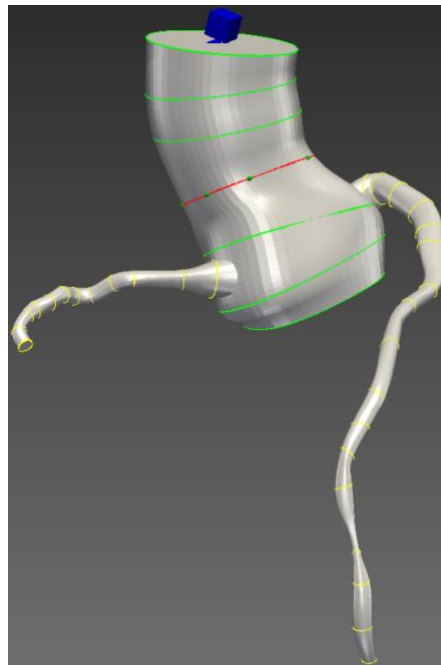


Figure 23. Vessel contours (color coded) and solid model (gray).

Chapter 4. Use of generated geometry in limited blood-flow simulations.

This chapter used the imaging data driven geometries to develop hemodynamic models of ten subjects. The following subsections consist of boundary conditions, followed by presentation of available 1D simulation results after which the 3D results are presented.

4.1 Boundary Conditions.

4.1.1 Aortic inflow boundary condition.

In all models, the inlet boundary conditions were imposed as transient left ventricular pressure. The left ventricular pressure profiles were obtained from the Haemod repository⁸⁷. The repository offers left ventricular pressure profiles at three different heart rates and in a range of systolic and diastolic pressures. In addition, a previous model from our laboratory⁴³ was also used to generate customized left ventricular pressure profiles. At each heart rate, six profiles from the profile were adopted in this study. As in the lumped parameter model presented in chapter 2, the spatially extended models presume centimeters-grams-seconds (CGS) units. Therefore, pressure in units of mmHg was converted to CGS units using a conversion factor of 1333.2. A representative left ventricular pressure profile is shown in **Figure 24**.

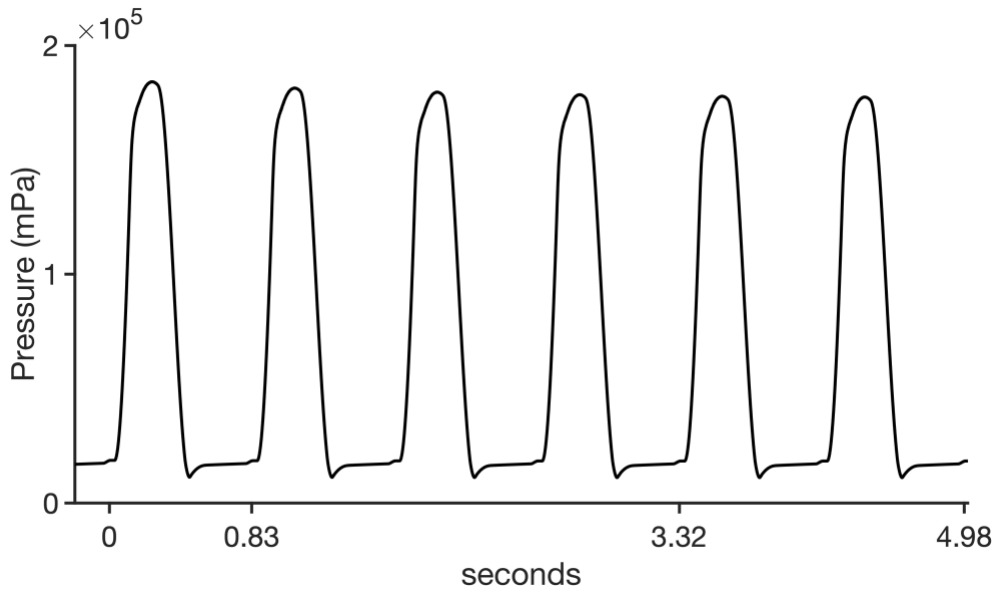


Figure 24. Representative left ventricular pressure profile from our previous study at a heart period of 0.83 s. The diastolic pressure is 26660 mPa and the systolic pressure is 181288 mPa. The conversion factor from mPa to mmHg is a factor 1.0/1333.2 mmHg/mPa .

4.1.2 Aortic outflow boundary condition.

The aortic outlet boundary conditions were modelled using a resistance-capacitance-resistance (RCR) Windkessel element. Model specific values using the geometries were estimated. In the Windkessel element, the first resistor R_p represents the proximal vasculature resistance, the capacitor C represents the vessel elasticity, and the second resistor R_d represents the microvasculature resistance. The RCR Windkessel element used in this study is illustrated in **Figure 25**.

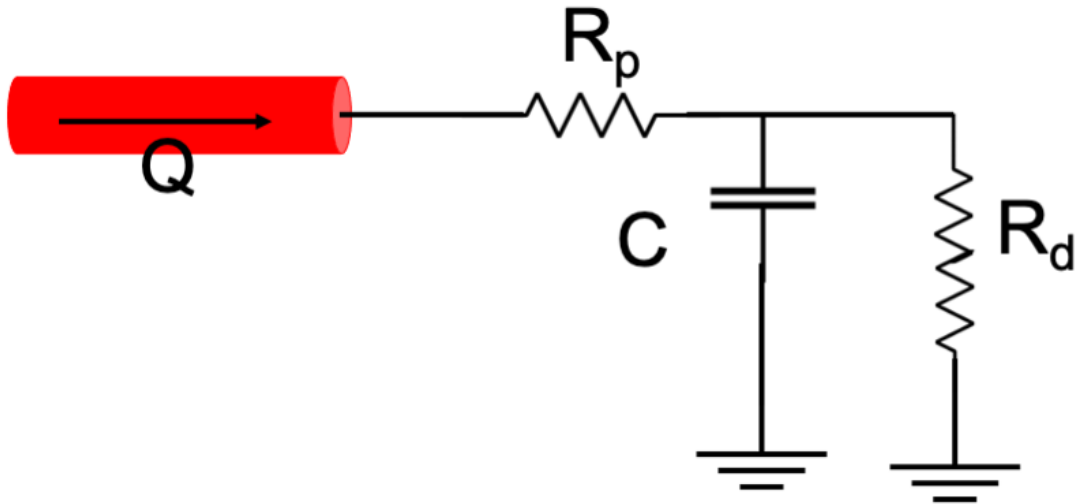


Figure 25. Resistor-Capacitor-Resistor (RCR) Windkessel unit used to represent the boundary condition for aortic outflow. The red tube represents a large vessel terminal through which the boundary condition receives a flow of Q . The arteriolar resistance is represented by R_p . Microvascular capacitance and resistance are represented by C and R_d respectively.

The elements that compose this model are the proximal resistance R_p , modeling the viscous resistance of the arterial vasculature just downstream of the model, a capacitor C which models the vessel compliance of all downstream vasculature, and the distal resistance R_d that models the resistance of the downstream capillaries and venous circulation. The terminal (total) resistance R_t is then a sum of both resistances:

$$R_t = R_p + R_d \quad \text{Equation (16).}$$

The value of R_t is calculated by

$$R_t = \frac{\bar{P}}{\bar{Q}} \quad \text{Equation (17).}$$

where \bar{P} is the mean pressure in dyne/cm² and Q is the cardiac output in cm³/s. The \bar{P} and the \bar{Q} were obtained from Kharche et al³⁹. The proximal resistance R_p is approximately 9% of R_t ⁸⁴⁻⁸⁶. The distal resistance R_d is approximately 91% of R_t . The capacitor in the RCR element representing the compliance of the blood vessel, modulates the amplitude of the pressure wave in the aorta, with increase values of capacitance translating to smaller amplitudes. As such, the aortic compliance value is tuned to allow for a systolic pressure of 120 mmHg and a diastolic pressure of 80mmHg. The baseline value is started at 0.001cm⁵/dyne and adjusted iteratively to obtain 120/80 aortic pressure range.

4.1.3 Coronary outflow boundary condition.

The boundary conditions for each of the coronary artery terminals is modelled using $R_a C_a R_{a\text{-micro}} C_{im} R_d$ Windkessel element (**Figure 26**). In addition to the resistances and capacitances, either the left ventricular pressure or the right ventricular pressure is also applied to mimic the cardiac contraction.

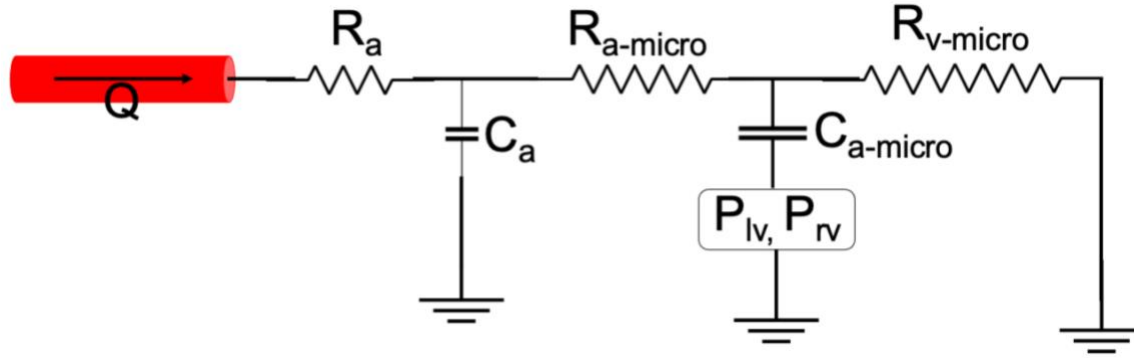


Figure 26. Components of coronary outflow boundary conditions consisting of proximal resistance R_a , arterial microvascular resistance $R_{a-micro}$, venous microvascular resistance $R_{v-micro}$, arterial compliance C_a , and microvascular compliance $C_{a-micro}$ used in spatially extended modelling.

Where R_a is the arterial resistance, $R_{a-micro}$ is the microcirculation resistance, $R_{v-micro}$ is the coronary venous microcirculation resistance, R_v is the venous resistance C_a is the coronary arterial compliance, C_{im} is the coronary myocardial compliance, and P_{im} is the time-varying intramyocardial pressure. To calculate the time varying intramyocardial pressure, the ventricular pressure signal (left or right as required) was used^{91,92}.

The total coronary resistance R_{cor} was taken to be 24 times that of the systemic vascular resistance, R_d , computed above^{91,92}. In each geometry, the cross sectional area, A_i , of each terminal was calculated. Using the cross sectional areas, each terminal was assigned a resistance as follows:

$$R_{cor,j} = \frac{\sum_j A_j^{1.3}}{A_i^{1.3}} R_{cor} \quad \text{Equation (18)}$$

Using $R_{cor,i}$, R_a , R_{amicro} , and R_v , were assigned following values:

done by Sankaran et al., where

$$R_a = 0.32 \times R_{cor};$$

$$R_{a,micro} = 0.52 \times R_{cor}; \quad \text{Equation (19)}$$

$$R_{v,micro} = 0.16 \times R_{cor};$$

Next, the capacitances for each coronary vessel were estimated. To do so, a total left coronary compliance of $3.6 \times 10^{-5} \text{ cm}^5/\text{dyne}$ ($C_{cor,L}$) was assumed, while a right coronary total compliance of $2.5 \times 10^{-5} \text{ cm}^5/\text{dyne}$ ($C_{cor,R}$) was assumed. Using the left or right total compliances, each terminal was assigned a compliance $C_{cor,i}$ as

$$C_{cor,i} = \frac{A_i}{\sum_j A_j} C_{cor,\{L,R\}} \quad \text{Equation (20)}$$

C_a is 11% of $C_{cor,i}$ for each terminal, while $C_{a-micro}$ is 89% of $C_{cor,i}$.

An alternate method to calculate these parameters is to first estimate that 4% of cardiac output is supplies the coronary arteries⁹³ while the remaining blood flows through the thoracic aorta. As the coronary arteries and aorta are in parallel, we have:

$$\frac{1}{R_{total}} = \frac{1}{R_{cor}} + \frac{1}{R_{ao}} \quad \text{Equation (21)}$$

We describe the flow split between the aorta and coronary arteries as:

$$Q_{cor} = \beta Q_{ao} \quad \text{Equation (22)}$$

where β is 0.04. Combining these two equations, we obtain the following two equations:

$$R_{cor} = \frac{1 + \beta}{\beta} R_{total} \quad \text{Equation (23)}$$

$$R_{ao} = (1 + \beta) R_{total}$$

The flow split γ to the left and right coronary arteries obtain the equations:

$$\gamma = \frac{Q_{cor}^{right}}{Q_{cor}^{left}}$$

$$R_{cor}^{right} = \gamma R_{cor}^{left}$$

We choose a 70%-30% flow split between the left main coronary artery and right main coronary artery based on literature⁹⁰.

Extending these equations further:

$$R_{cor}^{left} = \frac{1 + \gamma}{\gamma} R_{cor}$$

Equation (25)

$$R_{cor}^{right} = (1 + \gamma) R_{cor}$$

4.2 Visual observation of radius.

The radii of coronary vessel in each network were examined similar to a clinical assessment. The radii in each of four coronary geometries are shown in **Figure 27**. In **Figure 27**, the capital “X” marks the locations where the radius is smaller than its immediate proximal and distal radii. In addition to stenosed coronaries, other pathological changes of radius were also observed. In **Figure 25, Model 0**, there is a sudden reduction in radius which is likely to promote hemodynamic instability. Focal stenosis can also be observed in **Model 2** by the sudden reduction in radius. In **Model 1** and **Model 4**, the prolonged reduction in radii in indicated locations followed by an increase to prior measurements suggests the presence of diffuse stenosis in the vessel. Through observation of **Model 3**, diffuse nor focal stenosis cannot be identified from radii alone. This suggests further investigation through blood flow simulation may be required to identify an occlusion.

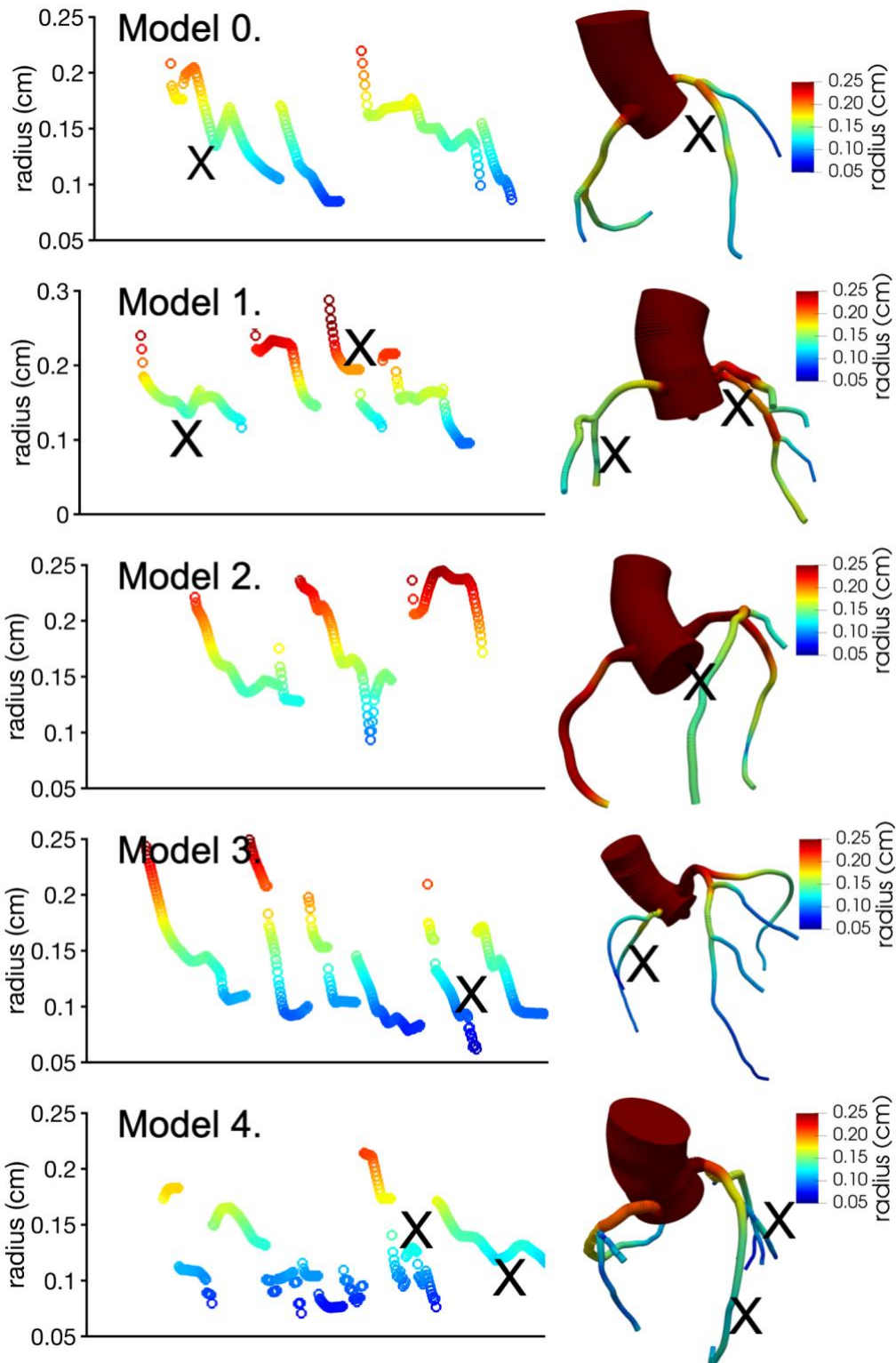


Figure 27. Coronary vessel radius in each of geometries 0 through 4. On each row, radius is plotted as a function of node number (left panel) and shown in a 3D

diagram (right panel). These representations may assist the user to identify a stenosis location. Locations of abnormal radius are marked as X in each panel where the user might expect unusual coronary flow behavior.

4.3 Hemodynamic 1D simulation.

Using the generated geometries and established boundary conditions, simple steady state simulations can be performed. An example of one 1D simulation is shown in **Figure 28**. Whereas **Panel A** shows the generated geometry (section 3), **Panel B** displays the 1D structure and corresponding FFR from a 1D steady state simulation.

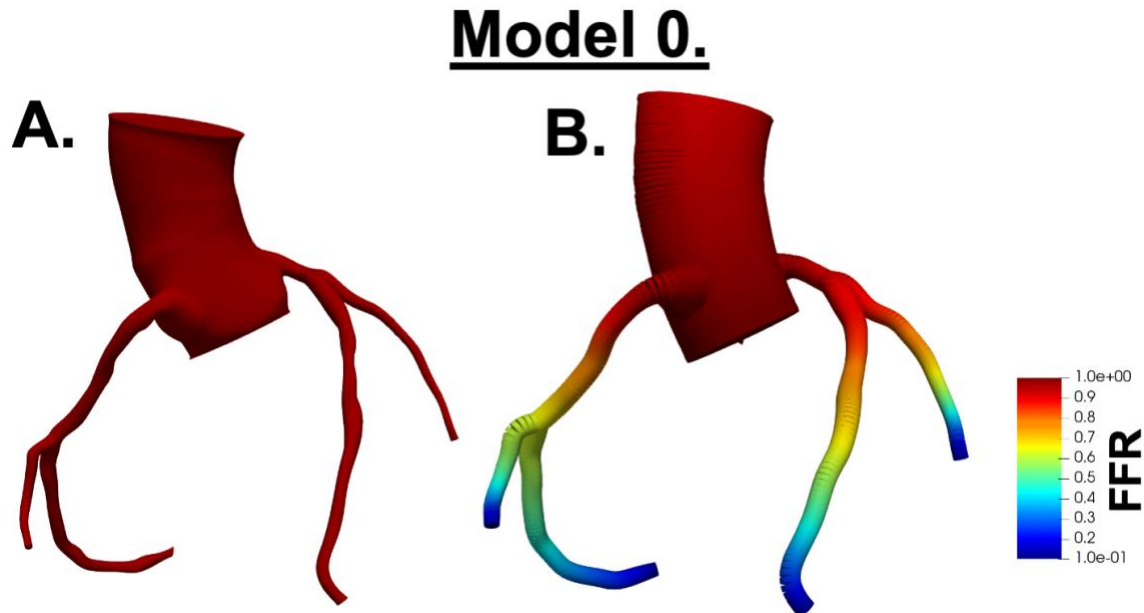


Figure 28. Steady state simulation for a 1D geometry. Panel A is the imaging driven construction of the 3D geometry. Panel B shows the estimated FFR.

Chapter 5. Discussion and Conclusions.

This thesis presented a mathematical model of the coronary vasculature capable of providing insights into coronary pathophysiology. The workflow that generated higher dimensional computational geometries from coronary CT imaging was also delivered.

5.1 Discussion of lumped parameter model findings.

A biophysical study of coronary hemodynamics is essential to gain deeper understanding of the underlying pathophysiology in the hope that the knowledge may lead to effective treatments. In line with the current worldwide focus of personalized medicine, biophysical studies may provide indication on how to do so. Prior to animal experiments and clinical trials, mathematical modelling is the most cost-effective start of an effective personalization process. Building on extant knowledge, this thesis further developed a coronary vasculature model and used it to investigate factors that affect FFR.

Judd and Mates⁹⁵ were one of the first to develop a simple model from experimental patient data that unveiled the out of phase nature of coronary flow with respect to the rest of the cardiovascular system. Their results suggest that the systolic decrease of coronary flow was impeded by some form of pressure rather than a transient increase in coronary resistance. The phenomenon has since been demonstrated in animal models by several researchers^{96,97}. In another study, Pietrabissa et al²⁸ developed a model to investigate the hemodynamics in coronary arteries before and after surgical bypass procedures. The approach of confirming surgery efficacy by computationally testing perioperative hemodynamic stability may become routine clinical practice⁹⁸. Further, the coronary-myocardium interaction mechanisms have been amply demonstrated in the experimental-modelling study in the Kassab group⁹⁹. Shim et al¹⁰⁰ coupled a full body cardiovascular

system lumped parameter model to a local model of the coronary circulation and investigated the effects of introducing stenosis within an artery. Their findings showed that the coupling of the systems provide boundary conditions that slightly augment the predicted drop in flow rate through stenosed arteries. Duanmu et al²⁹ developed a lumped parameter representation of the coronary vasculature from patient CT image data coupled to a simple systemic circulation system. Their inclusion of head loss at the inlets of coronary vessels, where sudden changes in diameter occur, showed to significantly improve the accuracy of their pressure and flow profiles. In addition, they imposed stenoses in their models and computed FFR through stenoses. Their study demonstrated the value of the lumped parameter approach without recourse to time and resource consuming higher order models. Similar to the presented studies, modern models provide into the physiological mechanisms involved in routine clinical testing. For instance, Arthurs et al.¹⁰¹ demonstrated the role of metabolic feedback and adrenergic feedforward mechanisms on coronary flow during exercise testing. With each development of lumped parameter models for coronary vasculature, the value of computationally efficient models is becoming more apparent.

The work in this thesis investigated the effects of varying stenosis severity (structure) and microvascular dysfunction (function) on FFR estimation. We further developed a model of the coronary vasculature by coupling it to a full body human circulation model⁴² and including a detailed description of the coronary microvasculature³⁰. We investigated focal stenosis severity (reduction in diameter) and diffuse stenosis severity (length of stenosis through the blood vessel). Our findings showed that the detrimental effects on flow and maximum flow were most impacted by the severity of focal stenosis relative to the severity

of diffuse stenosis. Although diffuse stenosis resulted in a decrease in flow through the coronaries, clinically significant FFR to indicate the need for intervention was only apparent with a large reduction in diameter. A previous investigation into the importance of diffuse coronary atherosclerosis in the absence of focal stenosis showed that while diffuse stenosis is generally considered non-flow limiting, it results in a continuous gradual drop in pressure along the arterial length¹⁰². This graded resistance to flow can promote myocardial ischemia and the absence of a low FFR as shown in our results should be taken into consideration for clinical decision making.

For patients with severe focal stenosis, lumped parameter models are an effective tool in estimating FFR and aiding clinical decision. However, the effects of microvascular disease on FFR have not been investigated despite studies calling for the necessity of incorporating microvascular status in the interpretation of FFR¹⁰³.

5.2 Discussion of image processing to generate geometry.

The reverse engineering process of generating spatially extended models from imaging data has allowed for in silico investigations into the underlying physiological processes of arterial vasculature and circulation. This multi-dimensional and multi-disciplinary approach presents theoretical modelling as a high utility technique to aid in clinical decision making.

Although there are various pipelines to generate imaging based models, a challenge in all methods is the bottleneck of building patient specific models. In addition to the accuracy of these models and the ease of their generation, a critical component of these tools' utility for clinical decision making is the timely generation of results made readily available¹⁰⁴.

The image processing used in this thesis is inspired the technique introduced by Wang et al in 1999¹⁰⁵. This technique improved upon the method of using image level threshold for segmentation by allowing for an operator to construct the segmentation of 2D images from a 3D stack. The 2D images are generated by extracting perpendicular cross sections oriented along a vessel path. Although this method allows for the generation of spatially extended models ready for computational fluid dynamic simulations, it is flawed by the described time taken to process and the inter-operator variability.

The revolutionary advantage of machine learning and artificial intelligence has presented a valuable tool that can aid in alleviating the bottleneck of segmentation in generating patient specific models. Significant development in recent years on machine learning investigations show promise of techniques to improve generation of image-based models through time and accuracy.

Although many methods have been developed to extract centrelines from imaging data^{106–109}, they all require assistance from an operator to ensure accuracy and relevance of extracted vessels.

Cheung et al¹¹⁰ proposed a fully automated machine learning model to segment the aorta and coronary arteries. The performance of their proposed model showed high accuracy and comparable to existing models. The value of their model however, is their lack of requiring high algorithmic and graphical processing units, allowing for use in hospital settings.

5.3 A discussion of spatially extended (1D and 3D) modelling of fractional flow reserve and its applications.

Current practice of combining CCTA with CFD necessitates the development of reliable spatially extended (1D and 3D) models of coronary hemodynamics. The computation of

coronary flow and pressure is enabled by quality of the CT image, a knowledge of cardiac output and aortic pressure, and of microvascular health status¹¹¹. In the absence of complete observations an uncertainty quantification of the boundary conditions and geometry becomes essential¹¹². The manner in which subject specific (patient specific) model parameters can be estimated has been demonstrated by Kim et al. and others^{92,113}. The nature of coronary arterial 3D structure that feeds specific myocardial perfusion distribution using steady state flow was explored by the McIntyre group¹¹⁴. The relationship between common clinical metrics such as cardiac output, ECG, heart rate to coronary hemodynamics has been demonstrated using 3D modelling¹¹⁵. A large number of clinical trials have been performed to validate existing FFR_{CT} estimation¹¹⁶. The most straightforward application of FFR_{CT} being to assess an isolated lesion's severity, a grading of complex lesion's is an obvious extension⁵⁹. Studies have validated their 3D CFD simulators using 3D printed geometries¹¹⁷. A significant benefit of computer modelling is that it may provide physiological insights into the hemodynamic phenomena that underlie coronary events. Clinically, patients present with a spectrum of conditions such as hypertension, arrhythmia, and ischemia. In addition, they undergo stress testing such as tilting of the head, exercise, and adenosine that mimics exercise. Simulating coronary flow has been used to demonstrate the differences in blood flow velocity and wall shear stress under normal and pathological conditions¹¹⁸. The relationship between coronary blood flow and arrhythmia has recently started to become clear using modelling¹¹⁹. Inclusion of feedback control and the phase difference between aortic and coronary flow may improve the clinical recommendations provided by the simulations¹⁰¹. It is relevant to assess the severity of large vessel stenosis using FFR_{CT}, and

simultaneously gain knowledge of microvascular health. Using clinical catheter measurements, 3D coronary flow simulations now provide both FFR_{CT} and an index of microvascular resistance called instantaneous wave free ratio¹²⁰. Further, a knowledge of the biomechanical properties of common plaques, rupture risk assessment is enabled by the FFR_{CT} models¹²¹. The effects of extra-coronary vessels such as the aorta on FFR can be deduced from coronary flow modelling¹²². Prior to surgery, abnormal wall shear stress can be estimated using detailed 3D modelling¹²³. In addition, perioperative assessments are feasible that provide success metrics for PCI and other surgery¹²⁴. Computational hemodynamics is now a key tool in translating animal studies to human¹²⁵. It can be appreciated that FFR technology can be applied to other organ vasculature such as the kidney¹²⁶ and liver where CFD will play a significant role.

However, it can be appreciated that spatially extended modelling has a large number of degrees of freedom, which cascades into significant computational cost. Reduced order models, such as presented in this thesis, may be more suited for research as well as clinician desktop applications. Knowledge gained from spatially extended modelling should be summarized into a reliable statistical predictor¹²⁷.

5.4 Future Work.

Using models to inform research and clinical practice shows promise in improving the future of healthcare. This thesis has considered an example of this approach by developing an informative coronary model that describes coronary flow-pressure response to microvascular (boundary conditions) alterations. The limitations and assumptions made throughout the development of the thesis should be addressed for future progress.

An obvious next step is to implement the workflow for model personalization ¹²⁸. It is expected to involve estimation of model parameters using a sufficient number of subject specific signals. It should however be borne in mind that optimization procedures are computationally intensive, in addition to requiring high quality inputs¹²⁹.

This thesis partially addressed the use of subject specific data in the form of CT images to generate computational geometries. Further routinely acquired data may assist the parameter estimation. For example, model predictive capability will be enhanced if arterial age (i.e. levels of arterial calcification) are known. Although the use of multi-modal data is desirable¹³⁰, it is expected to be a job to bring it all together into one model. In addition, multi-modal data itself may be heterogeneous and inconsistent as using in silico models to inform personalised medicine shows great promise to advance the future of healthcare. This thesis considers an example of this approach describing the development, and use, of a patient-specific cardiovascular model to describe the adenosine response. The limitations and assumptions made throughout the development of the project need to be addressed if further progress is to be made.

A simplistic argument may lead to use of complex models. However, the predictive capability of the complex model will reduce because several of its parameters may remain uncertain or unidentified. Future development of the model will be based upon suitable uncertainty analysis¹³¹ inclusion of relevant mechanisms. Since the model parameters will invariably be different among subjects, uncertainty analysis will also provide a means of simulating populations. Simulation of populations is an upcoming field based on Gaussian processes¹³².

As it stands, the model is provided as a collection of functions in multiple programming languages (C, MATLAB, bash, python). Future work will make the code more modular and provide documentation for each part. For the benefit of future users, the code will be packaged with its documentation and dependencies to ensure successful uptake. The optimal approach will be to encode the current model into our version of the SimVascular platform.

Although lumped parameter modelling has its advantages, it may be incapable of providing a realistic prediction. The effects of vessel curvature may be difficult to account for. Additionally, emergent behaviour such as pulse wave velocity is inaccessible to lumped parameter modelling. The helical flow of blood through vessels cannot be simulated using 0D models. Blood flow may become turbulent especially under uneven stenosis conditions. Future work will use the outcomes of Chapter 3 and investigate coronary hemodynamics in 1D and 3D models. Regardless, our model may provide preliminary data and generate testable hypothesis for future clinical-computational studies.

5.5 Conclusions.

As fractional flow reserve continues to be the gold standard for quantifying the severity of coronary stenosis, the factors affecting the measurement are important to determine. This thesis tested the hypothesis that a prime regulator of FFR is the presence of microvascular disease (**H1**). The importance of diffuse stenosis relative to focal stenosis on FFR estimation was also compared (**H2**). Finally, the use of sensitivity analysis to reveal other factors affecting FFR was also determined (**H3**). These hypotheses were tested by developing a lumped parameter model of the coronary vasculature and implementing computational fluid dynamics to explore hemodynamic function (**Aim 1**).

The results suggest that both focal and diffuse stenosis are a primary regulator of FFR estimation and the identification of diffuse stenosis must be considered in clinical decision making. An important finding of this work is the effect of microvascular disease on FFR estimation. Although the effect of microvascular disease on FFR is not linear, the consideration of downstream microvasculature dysfunction on the necessary supply of blood through the coronaries is imperative. Another objective of this thesis (**Aim 2**) was to generate computational geometries from CT imaging data. Using free, available software for image visualization, segmentation, and finite element meshing, ten geometries were developed using imaging data. The developed geometries and software are open source for all members of the lab and the university community. To further investigate the factors affecting FFR, computational fluid dynamic investigations using these spatially extended models (1D and 3D) are anticipated in the future.

Chapter 6. References.

1. Tarride J, Ma ML, Desmeules M, et al. A review of the cost of cardiovascular disease. 2009;25(6):195-202.
2. Leopold JA, Loscalzo J. Emerging role of precision medicine in cardiovascular disease. *Circ Res.* 2018;122(9):1302-1315. doi:10.1161/CIRCRESAHA.117.310782
3. Ahmadi A, Stone GW, Leipsic J, et al. Association of coronary stenosis and plaque morphology with fractional flow reserve and outcomes. *JAMA Cardiol.* 2016;1(3):350-357. doi:10.1001/jamacardio.2016.0263
4. Melchionna S, Amati G, Bernaschi M, et al. Risk assessment of atherosclerotic plaques based on global biomechanics. *Med Eng Phys.* 2013;35(9):1290-1297. doi:10.1016/j.medengphy.2013.02.002
5. Marsden AL. Simulation based planning of surgical interventions in pediatric cardiology. *Phys Fluids.* 2013;25(10). doi:10.1063/1.4825031
6. Usus A. Patient-Specific Blood Flow Modelling in Diagnosis of Coronary Artery Disease. Published online 2016.
7. Fan L, Namani R, Choy JS, Kassab GS, Lee LC. Effects of Mechanical Dyssynchrony on Coronary Flow: Insights From a Computational Model of Coupled Coronary Perfusion With Systemic Circulation. *Front Physiol.* 2020;11. doi:10.3389/FPHYS.2020.00915/FULL
8. Scanlon PJ, Faxon DP, Audet AM, et al. *ACC/AHA Guidelines for Coronary Angiography. A Report of the American College of Cardiology/American Heart Association Task Force on Practice Guidelines (Committee on Coronary*

- Angiography*). Vol 33. Elsevier Masson SAS; 1999. doi:10.1016/S0735-1097(99)00126-6
9. Berman DS, Hachamovitch R, Leslee ;, et al. Roles of Nuclear Cardiology, Cardiac Computed Tomography, and Cardiac Magnetic Resonance: Assessment of Patients with Suspected Coronary Artery Disease*. Accessed March 13, 2022. http://www.snm.org/ce_online
 10. Machac J. Cardiac Positron Emission Tomography Imaging Why Cardiac Positron Emission Tomography (PET)? Published online 2005. doi:10.1053/j.semnuclmed.2004.09.002
 11. Nandalur KR, Dwamena BA, Choudhri AF, Nandalur MR, Carlos RC. Diagnostic performance of stress cardiac magnetic resonance imaging in the detection of coronary artery disease: a meta-analysis. *J Am Coll Cardiol*. 2007;50(14):1343-1353. doi:10.1016/J.JACC.2007.06.030
 12. Jaarsma C, Leiner T, Bekkers SC, et al. Diagnostic performance of noninvasive myocardial perfusion imaging using single-photon emission computed tomography, cardiac magnetic resonance, and positron emission tomography imaging for the detection of obstructive coronary artery disease: a meta-analysis. *J Am Coll Cardiol*. 2012;59(19):1719-1728. doi:10.1016/J.JACC.2011.12.040
 13. Van Hamersvelt RW, Voskuil M, De Jong PA, Willeminck MJ, Išgum I, Leiner T. Diagnostic performance of on-site coronary CT angiography–derived fractional flow reserve based on patient-specific lumped parameter models. *Radiol Cardiothorac Imaging*. 2019;1(4). doi:10.1148/RYCT.2019190036
 14. Casella G, Klauss V, Ottani F, Siebert U, Sangiorgio P, Bracchetti D. Impact of

- intravascular ultrasound-guided stenting on long-term clinical outcome: A meta-analysis of available studies comparing intravascular ultrasound-guided and angiographically guided stenting. *Catheter Cardiovasc Interv.* 2003;59(3):314-321. doi:10.1002/CCD.10537
15. Moussa ID, Jaff MR, Mehran R, et al. PERIPHERAL VASCULAR DISEASE Original Studies Prevalence and Prediction of Previously Unrecognized Peripheral Arterial Disease in Patients With Coronary Artery Disease: The Peripheral Arterial Disease in Interventional Patients Study. doi:10.1002/ccd.21969
 16. Jang IK, Bouma BE, Kang DH, et al. Visualization of coronary atherosclerotic plaques in patients using optical coherence tomography: comparison with intravascular ultrasound. *J Am Coll Cardiol.* 2002;39(4):604-609. doi:10.1016/S0735-1097(01)01799-5
 17. Bom MJ, Driessen RS, Kurata A, et al. Diagnostic value of comprehensive on-site and off-site coronary CT angiography for identifying hemodynamically obstructive coronary artery disease. *J Cardiovasc Comput Tomogr.* 2021;15(1):37-45. doi:10.1016/J.JCCT.2020.05.002
 18. Lee KE, Lee SH, Shin ES, Shim EB. A vessel length-based method to compute coronary fractional flow reserve from optical coherence tomography images. *Biomed Eng Online.* 2017;16(1):1-14. doi:10.1186/s12938-017-0365-4
 19. Zhang J, Zhong L, Luo T, et al. Simplified Models of Non-Invasive Fractional Flow Reserve Based on CT Images. Published online 2016:1-20. doi:10.1371/journal.pone.0153070
 20. Pontone G, Weir-McCall JR, Baggiano A, et al. Determinants of rejection rate for

- coronary CT angiography fractional flow reserve analysis. *Radiology*. 2019;292(3):597-605. doi:10.1148/radiol.2019182673
21. Gaur S, Achenbach S, Leipsic J, et al. Rationale and design of the HeartFlowNXT (HeartFlow analysis of coronary blood flow using CT angiography: NeXt sSteps) study. *J Cardiovasc Comput Tomogr*. 2013;7(5):279-288. doi:10.1016/J.JCCT.2013.09.003
 22. Joseph JJ, Lee TY, Goldman D, McIntyre CW, Kharche SR. The Role of Extra-Coronary Vascular Conditions that Affect Coronary Fractional Flow Reserve Estimation. *Lect Notes Comput Sci (including Subser Lect Notes Artif Intell Lect Notes Bioinformatics)*. 2021;12738 LNCS:595-604. doi:10.1007/978-3-030-78710-3_57
 23. Hoole SP, Seddon MD, Poulter RS, Mancini GBJ, Wood DA, Saw J. Fame comes at a cost: A Canadian analysis of procedural costs in use of pressure wire to guide multivessel percutaneous coronary intervention. *Can J Cardiol*. 2011;27(2):262.e1-262.e2. doi:10.1016/j.cjca.2010.12.019
 24. Tanigaki T, Emori H, Kawase Y, et al. QFR Versus FFR Derived From Computed Tomography for Functional Assessment of Coronary Artery Stenosis. *JACC Cardiovasc Interv*. 2019;12(20):2050-2059. doi:10.1016/J.JCIN.2019.06.043
 25. Charytan DM, Skali H, Shah NR, et al. Coronary flow reserve is predictive of the risk of cardiovascular death regardless of chronic kidney disease stage. *Kidney Int*. 2018;93(2):501-509. doi:10.1016/J.KINT.2017.07.025/ATTACHMENT/C546199C-4995-4FB6-BCFB-2FE885A7AE1A/MMC4.DOCX
 26. Ng MKC, Yong ASC, Ho M, et al. The index of microcirculatory resistance predicts

- myocardial infarction related to percutaneous coronary intervention. *Circ Cardiovasc Interv.* 2012;5(4):515-522. doi:10.1161/CIRCINTERVENTIONS.112.969048
27. Sagawa K, Lie RK, Schaefer J. Translation of Otto Frank's paper "Die Grundform des Arteriellen Pulses" Zeitschrift für Biologie 37: 483-526 (1899). *J Mol Cell Cardiol.* 1990;22(3):253-254. doi:10.1016/0022-2828(90)91459-K
 28. Pietrabissa R, Mantero S, Marotta T, Menicanti L. A lumped parameter model to evaluate the fluid dynamics of different coronary bypasses. *Med Eng Phys.* 1996;18(6):477-484. doi:10.1016/1350-4533(96)00002-1
 29. Duanmu Z, Yin M, Fan X, Yang X, Luo X. A patient-specific lumped-parameter model of coronary circulation. *Sci Rep.* 2018;8(1). doi:10.1038/S41598-018-19164-W
 30. Olufsen MS. Structured tree outflow condition for blood flow in larger systemic arteries. Published online 2019:257-268.
 31. Joseph JJ, Sun C, Lee T-Y, Goldman D, Kharche SR, McIntyre CW. Structure (Epicardial Stenosis) and Function (Microvascular Dysfunction) that Influences Coronary Fractional Flow Reserve Estimation. Published online March 2, 2022:21-25. doi:10.20944/PREPRINTS202203.0050.V1
 32. Serban R, Hindmarsh AC. Example Programs for ccodes v5.7.0. Published online 2021.
 33. Avolio AP. Multi-branched model of the human arterial system. *Med Biol Eng Comput* 1980 186. 1980;18(6):709-718. doi:10.1007/BF02441895
 34. Duanmu Z, Chen W, Gao H, Yang X, Luo X, Hill NA. A One-Dimensional

- Hemodynamic Model of the Coronary Arterial Tree. *Front Physiol.* 2019;10(July):1-12. doi:10.3389/fphys.2019.00853
35. Tretyakova RM, Lobov GI, Bocharov GA. Modelling lymph flow in the lymphatic system: From 0D to 1D spatial resolution. *Math Model Nat Phenom.* 2018;13(5). doi:10.1051/mmnp/2018044
 36. Sochi T. One-Dimensional Navier-Stokes Finite Element Flow Model. Published online April 8, 2013. doi:10.48550/arxiv.1304.2320
 37. Updegrave A, Wilson NM, Merkow J, Lan H, Marsden AL, Shadden SC. SimVascular: An Open Source Pipeline for Cardiovascular Simulation. *Ann Biomed Eng.* 2017;45(3):525-541. doi:10.1007/s10439-016-1762-8
 38. Updegrave A, Wilson NM, Merkow J, Lan H, Marsden AL, Shadden SC. SimVascular: An Open Source Pipeline for Cardiovascular Simulation. *Ann Biomed Eng.* 2017;45(3):525. doi:10.1007/S10439-016-1762-8
 39. Taylor CA, Hughes TJR, Zarins CK. Finite element modeling of blood flow in arteries. *Comput Methods Appl Mech Eng.* 1998;158(1-2):155-196. doi:10.1016/S0045-7825(98)80008-X
 40. Ross C, Steinman DA. EXACT FULLY 3D NAVIER-STOKES SOLUTIONS FOR BENCHMARKING. *Int J Numer METHODS I N FLUJDS.* 1994;19:369-375.
 41. Boileau E, Nithiarasu P, Blanco PJ, et al. BENCHMARK PAPER : ORIGINAL ARTICLE AND SUPPORTING DATASETS A benchmark study of numerical schemes for one-dimensional arterial blood flow modelling. 2015;(July):1-33. doi:10.1002/cnm
 42. Joseph JJ, Hunter TJ, Sun C, Goldman D, Kharche SR, McIntyre CW. Using a

- Human Circulation Mathematical Model to Simulate the Effects of Hemodialysis and Therapeutic Hypothermia. *Appl Sci* 2022, Vol 12, Page 307. 2021;12(1):307. doi:10.3390/APP12010307
43. Altamirano-Diaz L, Kassay AD, Serajelahi B, McIntyre CW, Filler G, Kharche SR. Arterial Hypertension and Unusual Ascending Aortic Dilatation in a Neonate With Acute Kidney Injury: Mechanistic Computer Modeling. *Front Physiol.* 2019;10:1391. doi:10.3389/FPHYS.2019.01391/BIBTEX
 44. Pijls NHJ, Fearon WF, Tonino PAL, et al. Fractional flow reserve versus angiography for guiding percutaneous coronary intervention in patients with multivessel coronary artery disease: 2-year follow-up of the FAME (Fractional Flow Reserve Versus Angiography for Multivessel Evaluation) study. *J Am Coll Cardiol.* 2010;56(3):177-184. doi:10.1016/J.JACC.2010.04.012
 45. Pijls NHJ, Van Gelder B, Van Der Voort P, et al. Fractional flow reserve. A useful index to evaluate the influence of an epicardial coronary stenosis on myocardial blood flow. *Circulation.* 1995;92(11):3183-3193. doi:10.1161/01.CIR.92.11.3183
 46. Fearon WF, Tonino PAL, De Bruyne B, Siebert U, Pijls NHJ. Rationale and design of the Fractional Flow Reserve versus Angiography for Multivessel Evaluation (FAME) study. *Am Heart J.* 2007;154(4):632-636. doi:10.1016/J.AHJ.2007.06.012
 47. Fearon WF, Bornschein B, Tonino PAL, et al. Economic evaluation of fractional flow reserve-guided percutaneous coronary intervention in patients with multivessel disease. *Circulation.* 2010;122(24):2545-2550. doi:10.1161/CIRCULATIONAHA.109.925396
 48. Patricio L, Tonino PAL, De Bruyne B, et al. Fractional flow reserve versus

- angiography for guiding percutaneous coronary intervention. *Rev Port Cardiol.* 2009;28(2):229-230. doi:10.1056/NEJMOA0807611
49. Ball C, Pontone G, Rabbat M. Fractional Flow Reserve Derived from Coronary Computed Tomography Angiography Datasets: The Next Frontier in Noninvasive Assessment of Coronary Artery Disease. *Biomed Res Int.* 2018;2018. doi:10.1155/2018/2680430
 50. Jeremias A, Stone GW. Fractional Flow Reserve for the Evaluation of Coronary Stenoses. *Catheter Cardiovasc Interv.* 2015;85(4):602-603. doi:10.1002/CCD.25851
 51. Odudu A, Francis ST, McIntyre CW. MRI for the assessment of organ perfusion in patients with chronic kidney disease. *Curr Opin Nephrol Hypertens.* 2012;21(6):647-654. doi:10.1097/MNH.0B013E328358D582
 52. Taylor CA, Fonte TA, Min JK, City R, Angeles L. Computational Fluid Dynamics Applied to Cardiac Computed Tomography for Noninvasive Quantification of Fractional Flow Reserve Scientific Basis. 2013;61(22). doi:10.1016/j.jacc.2012.11.083
 53. Coenen A, Lubbers MM, Kurata A, et al. Fractional flow reserve computed from noninvasive CT angiography data: Diagnostic performance of an on-site clinicianoperated computational fluid dynamics algorithm. *Radiology.* 2015;274(3):674-683. doi:10.1148/RADIOL.14140992
 54. Arthurs CJ, Khlebnikov R, Melville A, et al. CRIMSON: An open-source software framework for cardiovascular integrated modelling and simulation. *PLoS Comput Biol.* 2021;17(5). doi:10.1371/JOURNAL.PCBI.1008881

55. McCullough JWS, Richardson RA, Patronis A, et al. Towards blood flow in the virtual human: efficient self-coupling of HemeLB. *Interface Focus*. 2021;11(1):20190119. doi:10.1098/RSFS.2019.0119
56. Randles A, Draeger EW, Bailey PE. Massively parallel simulations of hemodynamics in the primary large arteries of the human vasculature. *J Comput Sci*. 2015;9:70-75. doi:10.1016/J.JOCS.2015.04.003
57. Kharche SR, Lemoine S, Tamasi T, Hur L, So A, McIntyre CW. Therapeutic Hypothermia Reduces Peritoneal Dialysis Induced Myocardial Blood Flow Heterogeneity and Arrhythmia. *Front Med*. 2021;8:700824. doi:10.3389/FMED.2021.700824/FULL
58. Ghorbanniahassankiadeh A, Marks DS, LaDisa JF. With fractional flow reserve for intermediate multivessel coronary disease. *J Biomech Eng*. 2021;143(5). doi:10.1115/1.4049746/1096333
59. Vardhan M, Gounley J, Chen SJ, et al. Non-invasive characterization of complex coronary lesions. *Sci Reports 2021 111*. 2021;11(1):1-15. doi:10.1038/s41598-021-86360-6
60. Chandola G, Zhang J-M, Tan R-S, et al. Computed Tomography Coronary Angiography and Computational Fluid Dynamics Based Fractional Flow Reserve Before and After Percutaneous Coronary Intervention. *Front Bioeng Biotechnol*. 2021;9. doi:10.3389/FBIOE.2021.739667/TEXT
61. Jonášová A, Vimmr J. On the relevance of boundary conditions and viscosity models in blood flow simulations in patient-specific aorto-coronary bypass models. *Int j numer method biomed eng*. 2021;37(4):e3439. doi:10.1002/CNM.3439

62. Vignon-Clementel IE, Alberto Figueroa C, Jansen KE, Taylor CA. Outflow boundary conditions for three-dimensional finite element modeling of blood flow and pressure in arteries. *Comput Methods Appl Mech Eng*. 2006;195(29-32):3776-3796. doi:10.1016/J.CMA.2005.04.014
63. Hunter TJ, Joseph JJ, Anazodo U, Kharche SR, McIntyre CW, Goldman D. Atrial Fibrillation and Anterior Cerebral Artery Absence Reduce Cerebral Perfusion: A De Novo Hemodynamic Model. *Appl Sci* 2022, Vol 12, Page 1750. 2022;12(3):1750. doi:10.3390/APP12031750
64. Olufsen MS, Nadim A. On deriving lumped models for blood flow and pressure in the systemic arteries. *Comput Fluid Solid Mech* 2003. 2003;(1):1786-1789. doi:10.1016/B978-008044046-0.50436-X
65. Duanmu Z, Yin M, Fan X, Yang X, Luo X. A patient-specific lumped-parameter model of coronary circulation. *Sci Rep*. 2018;8(1):1-10. doi:10.1038/s41598-018-19164-w
66. Britton OJ, Bueno-Orovio A, Van Ammel K, et al. Experimentally calibrated population of models predicts and explains intersubject variability in cardiac cellular electrophysiology. Published online 2013. doi:10.1073/pnas.1304382110
67. Duanmu Z, Chen W, Gao H, Yang X, Luo X, Hill NA. A One-Dimensional Hemodynamic Model of the Coronary Arterial Tree. *Front Physiol*. 2019;10(July):1-12. doi:10.3389/fphys.2019.00853
68. Heldt T, Shim EB, Kamm RD, Mark RG, Massachusetts. Computational modeling of cardiovascular response to orthostatic stress. *J Appl Physiol*. 2002;92(3):1239-1254. doi:10.1152/japplphysiol.00241.2001

69. Marino S, Hogue IB, Ray CJ, Kirschner DE. A methodology for performing global uncertainty and sensitivity analysis in systems biology. *J Theor Biol.* 2008;254(1):178-196. doi:10.1016/j.jtbi.2008.04.011
70. Kharche SR, Lemoine S, Tamasi T, Hur L, So A, McIntyre CW. Therapeutic Hypothermia Reduces Peritoneal Dialysis Induced Myocardial Blood Flow Heterogeneity and Arrhythmia. *Front Med.* 2021;8. doi:10.3389/FMED.2021.700824
71. Jonášová A, Vimmr J. On the relevance of boundary conditions and viscosity models in blood flow simulations in patient-specific aorto-coronary bypass models. *Int j numer method biomed eng.* 2021;37(4). doi:10.1002/CNM.3439
72. Shim EB, Youn CH, Heldt T, Kamm RD, Mark RG. Computational modeling of the cardiovascular system after fontan procedure. *Lect Notes Comput Sci (including Subser Lect Notes Artif Intell Lect Notes Bioinformatics).* 2002;2526:105-114. doi:10.1007/3-540-36104-9_12
73. Heldt T. Computational models of cardiovascular response to orthostatic stress. Published online 2004:185. <http://dspace.mit.edu/handle/1721.1/28761>
74. GNU Parallel: The Command-Line Power Tool | USENIX. Accessed March 14, 2022. <https://www.usenix.org/publications/login/february-2011-volume-36-number-1/gnu-parallel-command-line-power-tool>
75. Chien S, Usami S, Taylor HM, Lundberg JL, Gregersen MI. Effects of hematocrit and plasma proteins on human blood rheology at low shear rates. *J Appl Physiol.* 1966;21(1):81-87. doi:10.1152/JAPPL.1966.21.1.81
76. Kolli KK, Banerjee RK, Peelukhana S V., et al. Influence of heart rate on fractional

- flow reserve, pressure drop coefficient, and lesion flow coefficient for epicardial coronary stenosis in a porcine model. *Am J Physiol Hear Circ Physiol*. 2011;300(1):H382-H387. doi:10.1152/ajpheart.00412.2010
77. Carlson BE, Arciero JC, Secomb TW. Theoretical model of blood flow autoregulation: Roles of myogenic, shear-dependent, and metabolic responses. *Am J Physiol - Hear Circ Physiol*. 2008;295(4):1572-1579. doi:10.1152/ajpheart.00262.2008
78. Lücker A, Secomb TW, Weber B, Jenny P. The relation between capillary transit times and hemoglobin saturation heterogeneity. Part 1: Theoretical models. *Front Physiol*. 2018;9(APR). doi:10.3389/FPHYS.2018.00420/FULL
79. Pries AR, Secomb TW. Microcirculatory network structures and models. *Ann Biomed Eng*. 2000;28(8):916-921. doi:10.1114/1.1308495
80. Clavica F, Alastruey J, Borlotti A, Sherwin SJ, Khir AW. One-dimensional computational model of pulse wave propagation in the human bronchial tree. *Annu Int Conf IEEE Eng Med Biol Soc IEEE Eng Med Biol Soc Annu Int Conf*. 2010;2010:2473-2476. doi:10.1109/IEMBS.2010.5626559
81. Poleszczuk J, Debowska M, Dabrowski W, Wojcik-Zaluska A, Zaluska W, Waniewski J. Patient-specific pulse wave propagation model identifies cardiovascular risk characteristics in hemodialysis patients. *PLoS Comput Biol*. 2018;14(9). doi:10.1371/JOURNAL.PCBI.1006417
82. Womersley JR. Oscillatory flow in arteries: The constrained elastic tube as a model of arterial flow and pulse transmission. *Phys Med Biol*. 1957;2(2):178-187. doi:10.1088/0031-9155/2/2/305

83. Marants R, Qirjazi E, Lai KB, et al. Exploring the Link Between Hepatic Perfusion and Endotoxemia in Hemodialysis. *Kidney Int Reports*. 2021;6(5):1336-1345. doi:10.1016/J.EKIR.2021.02.008
84. Updegrove A, Wilson NM, Merkow J, Lan H, Marsden AL, Shadden SC. SimVascular: An Open Source Pipeline for Cardiovascular Simulation. *Ann Biomed Eng*. 2017;45(3):525-541. doi:10.1007/s10439-016-1762-8
85. Bidgood WD, Horii SC, Prior FW, Van Syckle DE. Understanding and Using DICOM, the Data Interchange Standard for Biomedical Imaging. *J Am Med Informatics Assoc*. 1997;4(3):199-212. doi:10.1136/JAMIA.1997.0040199/2/JAMIA0040199.F06.JPEG
86. Sahni O, Kenneth AE, Ae EJ, Ae MSS, Ae CAT, Beall MW. Adaptive boundary layer meshing for viscous flow simulations. doi:10.1007/s00366-008-0095-0
87. Willemet M, Chowienczyk P, Alastruey J. A database of virtual healthy subjects to assess the accuracy of foot-to-foot pulse wave velocities for estimation of aortic stiffness. *Am J Physiol - Hear Circ Physiol*. 2015;309(4):H663-H675. doi:10.1152/AJPHEART.00175.2015/ASSET/IMAGES/LARGE/ZH4015151588A001.JPEG
88. Kim HJ, Vignon-Clementel IE, Figueroa CA, Jansen KE, Taylor CA. Developing computational methods for three-dimensional finite element simulations of coronary blood flow. *Finite Elem Anal Des*. 2010;46(6):514-525. doi:10.1016/J.FINEL.2010.01.007
89. Zhou Y, Kassab GS, Molloy S. On the design of the coronary arterial tree: A generalization of Murray's law. *Phys Med Biol*. 1999;44(12):2929-2945.

doi:10.1088/0031-9155/44/12/306

90. Sankaran S, Moghadam ME, Kahn AM, Tseng EE, Guccione JM, Marsden AL. Patient-specific multiscale modeling of blood flow for coronary artery bypass graft surgery. *Ann Biomed Eng.* 2012;40(10):2228-2242. doi:10.1007/S10439-012-0579-3
91. Kim HJ, Vignon-Clementel IE, Figueroa CA, et al. On coupling a lumped parameter heart model and a three-dimensional finite element aorta model. *Ann Biomed Eng.* 2009;37(11):2153-2169. doi:10.1007/s10439-009-9760-8
92. Kim HJ, Vignon-Clementel IE, Coogan JS, Figueroa CA, Jansen KE, Taylor CA. Patient-specific modeling of blood flow and pressure in human coronary arteries. *Ann Biomed Eng.* 2010;38(10):3195-3209. doi:10.1007/s10439-010-0083-6
93. Bogren HG, Klipstein RH, Firmin DN, et al. Quantitation of antegrade and retrograde blood flow in the human aorta by magnetic resonance velocity mapping. *Am Heart J.* 1989;117(6):1214-1222. doi:10.1016/0002-8703(89)90399-2
94. Johnson K, Sharma P, Oshinski J. Coronary artery flow measurement using navigator echo gated phase contrast magnetic resonance velocity mapping at 3.0 T. *J Biomech.* 2008;41(3):595-602. doi:10.1016/J.JBIOMECH.2007.10.010
95. Judd RM, Mates RE. Coronary input impedance is constant during systole and diastole. Published online 1991.
96. Spaan JAE, Breuls NPW, Laird JD. Diastolic-systolic coronary flow differences are caused by intramyocardial pump action in the anesthetized dog. *Circ Res.* 1981;49(3):584-593. doi:10.1161/01.RES.49.3.584
97. Sun Y, Gewirtz H. Estimation of intramyocardial pressure and coronary blood flow

- distribution. *Am J Physiol - Hear Circ Physiol.* 1988;255(3).
doi:10.1152/ajpheart.1988.255.3.h664
98. Marsden AL, Bernstein AJ, Reddy VM, et al. Evaluation of a novel Y-shaped extracardiac Fontan baffle using computational fluid dynamics. *J Thorac Cardiovasc Surg.* 2009;137(2). doi:10.1016/J.JTCVS.2008.06.043
99. Algranati D, Kassab GS, Lanir Y, Lanir Y. Mechanisms of myocardium-coronary vessel interaction. *Am J Physiol Hear Circ Physiol.* 2010;298:861-873. doi:10.1152/ajpheart.00925.2009.-The
100. Shim EB, Kamm RD, Heldt T, Mark RG. Numerical analysis of blood flow through a stenosed artery using a coupled multiscale simulation method. *Comput Cardiol.* Published online 2000:219-222. doi:10.1109/CIC.2000.898496
101. Arthurs CJ, Lau KD, Asrress KN, Redwood SR, Alberto Figueroa C. A mathematical model of coronary blood flow control: Simulation of patientspecific three-dimensional hemodynamics during exercise. *Am J Physiol - Hear Circ Physiol.* 2016;310(9):H1242-H1258. doi:10.1152/ajpheart.00517.2015
102. De Bruyne B, Hersbach F, Pijls NHJ, et al. Abnormal epicardial coronary resistance in patients with diffuse atherosclerosis but “normal” coronary angiography. *Circulation.* 2001;104(20):2401-2406. doi:10.1161/HC4501.099316/FORMAT/EPUB
103. Van De Hoef TP, Nolte F, Echavarría-Pinto M, et al. Impact of hyperaemic microvascular resistance on fractional flow reserve measurements in patients with stable coronary artery disease: insights from combined stenosis and microvascular resistance assessment. *Heart.* 2014;100(12):951-959. doi:10.1136/HEARTJNL-

2013-305124

104. Steinman DA, Taylor CA. Flow imaging and computing: Large artery hemodynamics. *Ann Biomed Eng.* 2005;33(12 SPEC. ISS.):1704-1709. doi:10.1007/S10439-005-8772-2
105. Wang KC, Dutton RW, Taylor CA. Improving geometric model construction for blood flow modeling: Geometric image segmentation and image-based model construction for computational hemodynamics. *IEEE Eng Med Biol Mag.* 1999;18(6):33-39. doi:10.1109/51.805142
106. . S, Khan SA, Hassan A, Rashid S. Blood Vessel Segmentation and Centerline Extraction based on Multilayered Thresholding in CT Images. Published online 2014:428-432. doi:10.12792/ICISIP2014.081
107. Maddah M, Soltanian-Zadeh H, Afzali-Kusha A. Snake modeling and distance transform approach to vascular centerline extraction and quantification. *Comput Med Imaging Graph.* 2003;27(6):503-512. doi:10.1016/S0895-6111(03)00040-5
108. Chen D, Cohen LD. Piecewise geodesics for vessel centerline extraction and boundary delineation with application to retina segmentation. *Lect Notes Comput Sci (including Subser Lect Notes Artif Intell Lect Notes Bioinformatics).* 2015;9087:270-281. doi:10.1007/978-3-319-18461-6_22
109. Santamaría-Pang A, Colbert CM, Saggau P, Kakadiaris IA. Automatic centerline extraction of irregular tubular structures using probability volumes from multiphoton imaging. *Med Image Comput Comput Assist Interv.* 2007;10(Pt 2):486-494. doi:10.1007/978-3-540-75759-7_59
110. Cheung WK, Bell R, Nair A, et al. A Computationally Efficient Approach to

- Segmentation of the Aorta and Coronary Arteries Using Deep Learning. *IEEE access Pract Innov open Solut.* 2021;9:108873-108888. doi:10.1109/ACCESS.2021.3099030
111. Taylor CA, Fonte TA, Min JK. Computational fluid dynamics applied to cardiac computed tomography for noninvasive quantification of fractional flow reserve: scientific basis. *J Am Coll Cardiol.* 2013;61(22):2233-2241. doi:10.1016/j.jacc.2012.11.083
112. Morbiducci U, Ponzini R, Gallo D, Bignardi C, Rizzo G. Inflow boundary conditions for image-based computational hemodynamics: impact of idealized versus measured velocity profiles in the human aorta. *J Biomech.* 2013;46(1):102-109. doi:10.1016/J.JBIOMECH.2012.10.012
113. Sankaran S, Kim HJ, Choi G, Taylor CA. Uncertainty quantification in coronary blood flow simulations: Impact of geometry, boundary conditions and blood viscosity. *J Biomech.* 2016;49(12):2540-2547. doi:10.1016/J.JBIOMECH.2016.01.002
114. Kharche SR, So A, Salerno F, et al. Computational assessment of blood flow heterogeneity in peritoneal dialysis patients' cardiac ventricles. *Front Physiol.* 2018;9(MAY). doi:10.3389/FPHYS.2018.00511/FULL
115. Malota Z, Glowacki J, Sadowski W, Kostur M. Numerical analysis of the impact of flow rate, heart rate, vessel geometry, and degree of stenosis on coronary hemodynamic indices. *BMC Cardiovasc Disord.* 2018;18(1). doi:10.1186/S12872-018-0865-6
116. Ball C, Pontone G, Rabbat M. Fractional Flow Reserve Derived from Coronary

- Computed Tomography Angiography Datasets: The Next Frontier in Noninvasive Assessment of Coronary Artery Disease. *Biomed Res Int.* 2018;2018. doi:10.1155/2018/2680430
117. Shepard L, Sommer K, Izzo R, et al. Initial Simulated FFR Investigation Using Flow Measurements in Patient-specific 3D Printed Coronary Phantoms. *Proc SPIE--the Int Soc Opt Eng.* 2017;10138:101380S. doi:10.1117/12.2253889
118. Hoque KE, Ferdows M, Sawall S, Tzirtzilakis EE. The effect of hemodynamic parameters in patient-based coronary artery models with serial stenoses: normal and hypertension cases. *Comput Methods Biomech Biomed Engin.* 2020;23(9):467-475. doi:10.1080/10255842.2020.1737028
119. Gamilov T, Kopylov P, Serova M, et al. Computational analysis of coronary blood flow: The role of asynchronous pacing and arrhythmias. *Mathematics.* 2020;8(8):1-16. doi:10.3390/MATH8081205
120. Ghorbanniahassankiadeh A, Marks DS, LaDisa JF. Correlation of Computational Instantaneous Wave-Free Ratio With Fractional Flow Reserve for Intermediate Multivessel Coronary Disease. *J Biomech Eng.* 2021;143(5). doi:10.1115/1.4049746
121. Kueh SH, Boroditsky M, Leipsic J. Fractional flow reserve computed tomography in the evaluation of coronary artery disease. *Cardiovasc Diagn Ther.* 2017;7(5):463-474. doi:10.21037/cdt.2017.01.04
122. Razavi MS, Shirani E, Kassab GS. Scaling laws of flow rate, vessel blood volume, lengths, and transit times with number of capillaries. *Front Physiol.* 2018;9(MAY):581. doi:10.3389/fphys.2018.00581

123. Chiastra C, Mazzi V, Lodi Rizzini M, et al. Coronary Artery Stenting Affects Wall Shear Stress Topological Skeleton. *J Biomech Eng.* 2022;144(6). doi:10.1115/1.4053503/1131202
124. Chandola G, Zhang J-M, Tan R-S, et al. Computed Tomography Coronary Angiography and Computational Fluid Dynamics Based Fractional Flow Reserve Before and After Percutaneous Coronary Intervention. *Front Bioeng Biotechnol.* 2021;9. doi:10.3389/FBIOE.2021.739667/BIBTEX
125. De Nisco G, Chiastra C, J Hartman EM, et al. Comparison of Swine and Human Computational Hemodynamics Models for the Study of Coronary Atherosclerosis. 2021;9:1. doi:10.3389/fbioe.2021.731924
126. Mandaltsi A, Grytsan A, Odudu A, et al. Non-invasive Stenotic Renal Artery Haemodynamics by in silico Medicine. *Front Physiol.* 2018;9(AUG):1106. doi:10.3389/fphys.2018.01106
127. Arzani A, Wang J-X, Sacks MS, Shadden SC. Machine Learning for Cardiovascular Biomechanics Modeling: Challenges and Beyond. *Ann Biomed Eng.* 2022;50(6):615-627. doi:10.1007/S10439-022-02967-4
128. Li B, Wang W, Mao B, Liu Y. A Method to Personalize the Lumped Parameter Model of Coronary Artery. *Int J Comput Methods.* 2019;16(3). doi:10.1142/S0219876218420045
129. Marsden AL. Optimization in Cardiovascular Modeling. <http://dx.doi.org/101146/annurev-fluid-010313-141341>. 2014;46:519-546. doi:10.1146/ANNUREV-FLUID-010313-141341
130. Csippa B, Üveges Á, Gyürki D, et al. Simplified coronary flow reserve calculations

- based on three-dimensional coronary reconstruction and intracoronary pressure data. *Cardiol J*. Published online September 30, 2021. doi:10.5603/CJ.A2021.0117
131. Steinman DA, Migliavacca F. Editorial: Special Issue on Verification, Validation, and Uncertainty Quantification of Cardiovascular Models: Towards Effective VVUQ for Translating Cardiovascular Modelling to Clinical Utility. *Cardiovasc Eng Technol* 2018 94. 2018;9(4):539-543. doi:10.1007/S13239-018-00393-Z
132. Melis A, Clayton RH, Marzo A. Bayesian sensitivity analysis of a 1D vascular model with Gaussian process emulators. *Int j numer method biomed eng*. 2017;33(12):1-11. doi:10.1002/cnm.2882

Curriculum Vitae.

Mr. Jermiah J. Joseph. B.Sc.

A. SUMMARY OF TECHNICAL SKILLS

- Programming and scientific visualization: Thorough knowledge of MATLAB, Java, Python, VTK, and C/C++ languages;
- scientific writing (thesis and manuscript drafting); and
- programming microcontrollers and building projects using Raspberry Pi.

B. EDUCATION

University of Western Ontario

Master of Science in Medical Biophysics

Class of 2022

- Expected completion August 2022.

**Bachelor of Science with an Honors Specialization in Integrated Science with
Computer Science (GPA = 3.88)** Class of 2020

- Completed courses equivalent to first year Chemistry, Biology, Physics, Computer Science, Earth Science, Astronomy, and Statistics as well as upper year Environmental Science, Algorithms, Operating Systems, Logic, Discrete Math, Big Data Modelling, and Philosophy.

C. AWARDS.

- Dean's Honors List 2017-2019.
- School of Medicine, Lawson Institute, Summer internship funding 2018-2020.
- NSERC CGSM award 2020-2021 (awarded).
- OGS award 2020-2021 (awarded).

D. PUBLICATIONS

Joseph, J.J.; Sun, C.; Lee, T.-Y.; Goldman, D.; Kharche, S.R.; McIntyre, C.W. Structure (Epicardial Stenosis) and Function (Microvascular Dysfunction) That Influence Coronary Fractional Flow Reserve Estimation. Appl. Sci. 2022, 12, 4281. <https://doi.org/10.3390/app12094281> . **Impact factor: 2.7.**

1. **Joseph, J.J.;** Hunter, T.J.; Sun, C.; Goldman, D.; Kharche, S.R.; McIntyre, C.W. Using a Human Circulation Mathematical Model to Simulate the Effects of Hemodialysis and Therapeutic Hypothermia. Appl. Sci. 2022, 12, 307. <https://doi.org/10.3390/app12010307>. Impact factor: 2.7.
2. **Joseph, J.J.,** Lee, TY., Goldman, D., McIntyre, C.W., Kharche, S.R. (2021). The Role of Extra-Coronary Vascular Conditions that Affect Coronary Fractional Flow Reserve Estimation. In: Ennis, D.B., Perotti, L.E., Wang, V.Y. (eds) Functional Imaging and Modeling of the Heart. FIMH 2021. Lecture Notes in Computer Science, vol 12738. Springer, Cham. https://doi.org/10.1007/978-3-030-78710-3_57.
3. Hunter, T.J.; **Joseph, J.J.;** Anazodo, U.; Kharche, S.R.; McIntyre, C.W.; Goldman, D. Atrial Fibrillation and Anterior Cerebral Artery Absence Reduce Cerebral Perfusion: A De Novo Hemodynamic Model. Appl. Sci. 2022, 12, 1750. <https://doi.org/10.3390/app12031750>
4. Hunter, T.J., **Joseph, J.J.,** Anazodo, U., Kharche, S.R., McIntyre, C.W., Goldman, D. (2021). Computational Modelling of the Role of Atrial Fibrillation on Cerebral Blood Perfusion. In: Ennis, D.B., Perotti, L.E., Wang, V.Y. (eds) Functional Imaging and Modeling of the Heart. FIMH 2021. Lecture Notes in Computer Science, vol 12738. Springer, Cham. https://doi.org/10.1007/978-3-030-78710-3_65
5. **J. J. Joseph,** C. W. McIntyre and S. R. Kharche, "Proarrhythmic Effects of

Electrolyte Imbalance in Virtual Human Atrial and Ventricular Cardiomyocytes," 2020 42nd Annual International Conference of the IEEE Engineering in Medicine & Biology Society (EMBC), 2020, pp. 2315-2318, doi: 10.1109/EMBC44109.2020.9176060.

6. Sanjay R. Kharche, Raanan Marants, Elena Qirjazi, Andrea D. Kassay, **Jermiah Joseph**, Kierra D. McDougall, Ting Lee, Christopher W. McIntyre. Understanding the Effects of Haemodialysis on Blood Flow: An Imaging-Mathematical Modelling Study. American Society of Nephrology Annual Conference. San Diego. 2018.
7. Sanjay R. Kharche, Wen Yao Xia, Andrea D. Kassay, **Jermiah Joseph**, Kierra D. McDougall, Terry M. Peters, Christopher W. McIntyre. Bioengineering Quantification of the Effects of a Haemodialysis Patient's Cardiac Ejection Fraction: Towards Patient Specific Risk Prediction. American Society of Nephrology Annual Conference. San Diego. 2018.
8. **Jermiah Joseph**, Katelyn Melo, Devanshi Shukla, Tony Nguyen, Katherine Teeter. Integrated Science 3002A: Big Bike Giveaway: Changing London's environment, health, and economy one bike at a time. Western Libraries. 2018.